University of Alberta

Library Release Form

Name of Author:	Hu Peng
Title of Thesis:	Microwave Sintering Process Model
Degree:	Master of Science
Year this Degree Granted:	2001

University of Alberta

MICROWAVE SINTERING PROCESS MODEL

By

HU PENG

©

A thesis submitted to the Faculty of Graduate Studies and Research in partial
fulfillment of the requirements for the degree of Master of Science

Department of Chemical and Materials Engineering

Edmonton, Alberta

Fall, 2001

University of Alberta

Faculty of Graduate Studies and Research

The undersigned certify that they have read, and recommend to the Faculty of Graduate Studies and Research for acceptance, a thesis entitled MICROWAVE SINTERING PROCESS MODEL submitted by Hu Peng in partial fulfillment of the requirements for the degree of Master of Science.

ABSTRACT

The microwave sintering ceramics and hardmetals technology is a prospective industrial technology which will have great advantages in short-time sintering and uniform heating. MicroWear Inc (now Indexable Cutting Tools) has successfully developed the microwave sintering silicon nitride and tungsten carbide processes. However, what really happens during the microwave sintering process is still largely unknown. The research work introduced in this thesis was focused on the measurement of the microwave power absorption properties of the materials involved in those processes and sequentially using the measurement data to simulate the real process.

The perturbation method as well as the attenuation method were employed to measure the dielectric properties of the susceptors, the silicon nitride green parts and the tungsten carbide green parts. Most tests are carried out through a big temperature range from room temperature to 800°C. These data were then used in the microwave heating process model to simulate the industrial process. The physical models are based on the microwave reflection at each interface between the materials and the microwave absorption in the bulk materials. Heat transfer between the components inside the sintering furnace has also been considered. Results from the simulated heating processes for both silicon nitride and tungsten carbide samples are close to those from the experimental data taking into account the lack of load rotation in the experimental time-temperature measurement.

By varying the parameters of the sintering furnace, such as the thickness of the

alumina tube wall, the thickness of the susceptor mixture layer, the sample load and the graphite plates load, the model data gives a simulated view of the effects of those parameters. These simulations are helpful to optimize the parameters in the real process.

ACKNOWLEDGEMENTS

CONTENTS

LIST OF TABLES

LIST OF FIGURES

LIST OF SYMBOLS

E	Electric field
H	Magnetic field
β	Phase constant
ε_0	Permittivity of free space
μ_0	Permeability of free space
ω	Frequency
v_p	Propagation speed
ε^*	Complex permittivity
μ^*	Complex permeability
λ	Wavelength
f	Frequency
f_0	Resonant frequency
Q	Quality factor
Q_0	Quality factor of empty resonator
Q_L	Quality factor with sample load
γ	Propagation constant
l	Sample length
ε'	Dielectric constant
ε''	Loss factor
α	Attenuation coefficient
T	Temperature
t	Time
P	Power
V	Volume
P_m	Power absorbed by susceptors in percentage relative to the total input power
P_s	Power absorbed by samples in percentage relative to the total input power
R	Reflected power in percentage relative to the total

	input Power
$\dot{q}_m$	Microwave power absorbed by the susceptors
$\dot{q}_s$	Microwave power absorbed by the samples
ρ	Density of material
ε	Emissivity
σ	Stefan-Boltzmann constant
	$(\sigma = 5.67 \times 10^{-8} W/m^2 K^4)$
K	Thermal Conductivity
A	Area
$q_{m\text{-}a}$	Heat transfer from the susceptors to the alumina tube
$q_{a\text{-}s}$	Heat transfer from the alumina tube to the samples
$q_{s\text{-}g}$	Heat transfer from the samples to the graphite plates
Δt	Time interval
C_p	Heat capacity of material
Q_s	Total heat generated to heat the samples
Q_a	Total heat generated to heat the alumina tube
Q_m	Total heat generated to heat the susceptors
Q_g	Total heat generated to heat the graphite plates
d	Thickness of the graphite plates

CHAPTER 1   MICROWAVE SINTERING TECHNOLOGY INTRODUCTION

Microwave sintering of silicon nitride tool bits has been successfully developed by the MicroWear Corp (recently purchased by the Indexable Cutting Tools) Also, the microwave sintering of tungsten carbide tool bits has been analyzed in recent years. However, what really happens during the microwave sintering process is still largely unknown. The goal of this project is to gain additional insight into these processes and to simulate the microwave sintering process including the heat generation by microwaves and the heat transfer within the furnace. This will allow us to predict the time temperature profile for a given microwave power and to optimize the furnace operation.

Microwave sintering technology has been developed and introduced into hard metal (cemented tungsten carbide) sintering processing recently. [1-5] Superior to the conventional sintering process, microwave sintering makes it possible to achieve a shorter sintering time and a lower sintering temperature. Hence, much smaller grain size and improved mechanical properties of parts are obtained by this process. Also, some special physical properties of certain ceramics such as superconductivity and piezoelectricity can be improved. Microwave heating can sinter almost all kinds of ceramic and semi-metal powders, and also, some pure metal powders can be sintered by microwave heating. [6]

1.1 Tungsten Carbide Conventional Sintering Techniques

Tungsten carbide bonded with metallic cobalt is termed hard metal or cemented tungsten carbide and is the first and most widely used cermet tool material. Sintered tungsten carbide tools and dies are a multibillion-dollar worldwide industry. Tungsten carbide tools not only have a superior hardness and toughness combination, but they also can operate at high temperature so they can be used at much higher cutting speed then ordinary tool steel.

Cemented carbides are manufactured by a powder metallurgy process consisting of a sequence of steps in which each step must be carefully controlled to obtain a final product with the desired properties, microstructure, and performance. The steps include:

1. Processing of the ore and the preparation of the tungsten carbide powder.
2. Preparation of the other carbide powders
3. Production (milling) of the powder grades
4. Compacting or powder consolidation
5. Sintering
6. Postsinter forming

The sintered product can be used directly or can be ground, polished and coated to suit a given application. [7]

Tungsten carbide powders are prepared by direct reduction of tungsten ore and then carburization from tungsten and carbon. The tungsten carbide powders are then mixed with binder powders, milled and dried. There are a wide variety of techniques used to compact the cemented carbide grade powders to the desired shape such as pill pressing, isostatic pressing and molding. Because of their poor compactability, tungsten carbide powders are usually compacted to only about 65% density. The green parts are then sintered to full density.

The sintering of tungsten carbide to full density is a critical stage in the process since it will directly determine the mechanical properties of the WC/Co products. Two basic methods are conventionally used to sinter cemented carbides: hydrogen sintering and vacuum sintering. Hydrogen sintering uses a hydrogen-based atmosphere at atmospheric pressure to dynamically control part composition. Vacuum sintering uses a vacuum or reduced-pressure environment to control composition through slowing of the reaction kinetics. [7] Sintering of cemented carbides consists of removal of pressing lubricant,

densification and microstructure development.

Several percent of lubricants are used for cemented carbide to reduce wear of the compacting dies. The lubricant can be removed at a few hundred degrees Celsius. The heating rate to remove the lubricants depends on the part size, lubricant type and content.

A densification curve for typical WC/Co shows that densification begins at 1000°C and that greater than 90% of theoretical density can be obtained at 1300°C. An important feature of the tungsten carbide-cobalt system is the high density attained in the very first stages of sintering. [8] Snowball [9] showed that cobalt flow into the carbide matrix occurs in the solid state, well below the melting point of the carbide-cobalt eutectic. But complete density can only be achieved in the final stage, which is liquid phase sintering. By a combination of initial solution and minimization of interfacial energy, close-packed junctions are formed between particles to give a major contribution to densification in the first, solution-rearrangement stage. At higher temperatures, mass transfer between carbide and cobalt leads to $W_xCo_yC_z$ alloy melting and results in liquid phase during the second stage of densification. Liquefaction occurs between 1280 and 1350°C, and the melt temperature depends on the compounds of the carbide/cobalt eutectic phase that are present. The liquid phase will first appear at the closest contacts between carbide and cobalt, because the thin slab at the carbide-cobalt interface will be the first region to achieve the eutectic point composition through diffusion. This liquid phase flows into the pores and wets the carbide particles to form a cobalt liquid net. Full density will be achieved soon after the liquid phase forms. The main purpose of the final stage of the sintering operation is to develop the microstructure by holding at a temperature above the $W_xCo_yC_z$ melting point for a certain time. During this period, the cobalt phase, driven by capillary forces, disperses more evenly. This process also improves the size distribution of carbide particles. On the other hand, prolonged sintering at this stage will lead to significant grain growth and sometimes results in density fall-off. The grain coarsening process is very sensitive to temperature and time. Vanadium carbide (VC), niobium carbide and/or tantalum carbides are added as grain growth inhibitors to prevent

discontinuous grain growth of the WC grains. Okada [10] investigated the addition of Cr_3C_2, and proposed that the retardation of grain growth during sintering by Cr_3C_2 addition was caused by the reduction of W flux through the Co phase. Carroll and Fox [11] showed that grain growth is strongly dependent on sintering temperature, grain growth inhibitor addition and the cobalt content of the WC/Co system. Lower sintering temperatures minimize grain growth and provide the broadest flexibility in terms of grain growth inhibitor selection. VC is much more effective as a grain growth inhibitor than Cr_3C_2. Additions of large amounts of the inhibitor carbide phases are detrimental to mechanical properties, reducing the toughness significantly because of the precipitation of brittle carbides at WC/Co interfaces. [12] During densification, the pressed part undergoes a volumetric shrinkage of about 40 to 45% (16 to 18% linear shrinkage). [13]

For the typical vacuum sintering process of WC/Co, the sintering peak temperature is 1450~1500°C, lubricant removal occurs during a hold at 450°C for 1 hour, degassing occurs during a hold at 1200°C for 45 min., and then sintering at 1450°C for 1 hour. The whole process will last 8~9 hours (including cooling time). Fig. 1.1 shows the conventional vacuum sintering process time-temperature cycle.
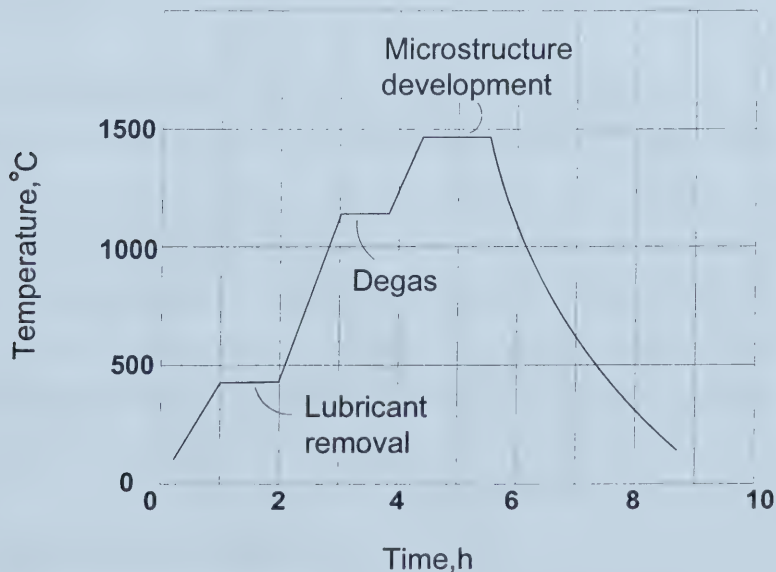
Fig. 1.1 Typical cemented carbide vacuum sinter time-temperature cycle

As Schubert [14] mentioned, the minimum grain size of WC in the conventional sintering process is 200-300 nm, while Sadangi reports a WC grain size in the range 20-50 nm using nanophase WC/Co alloy. The grain size ranges are shown in Fig. 1.2.


```
submicron hard                              nanophase
metals                                      hard metals

◄------                    ultrafine hard metals
conventional fine grained alloys

                                   alternative consolidation (flash
                                   sintering, forging, extrusion)

◄------    conventional liquid          ►       reaction milling of
           phase sintering                      elementary powders

                                   solid state
                                   sintering          atomic structure


1                  0.5                  0.2    0.1  0.05

WC grain size (um)
(schematic)
```
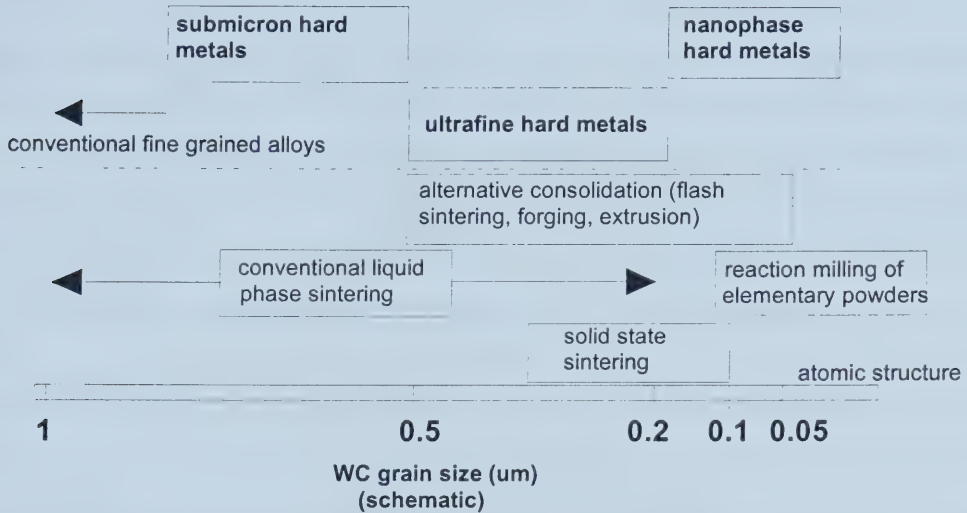
Fig. 1.2   Today's situation for fine grained hard metal manufacture and new trends for nanophase materials.[14]

The mechanical properties of WC/Co products highly depend on the grain size and final density, a smaller WC grain size with higher density will give a higher hardness and better wear properties. Conventional sintering has to find the optimal point at which the sintering time and temperature will produce good WC grain dispersion, high final density as well as a small grain size for maximum hardness. Obviously, it is difficult to find the optimal process parameters for the conventional process and realize them in production. Researchers are attempting to use smaller particles and different additives to get a smaller final grain size and still achieve full density.

1.2   Microwave Sintering Review

As a relatively new heating technology, microwave heating is being evaluated for the

cemented carbide sintering process. Superior to the conventional sintering processes, microwave sintering processes can give more uniform heating and higher heating rates.

In conventional sintering, the parts inside the furnace are heated indirectly by the absorption of the infrared radiation emitted by the heating element refractors and the neighboring parts and also by heat convection and conduction. In such a process the parts, i.e. the furnace load, are heated from the outside in. The temperature gradients within a part or within a furnace load are mainly determined by the thermal conductivity and emissivity of the parts. There is a maximum allowed temperature gradient within the parts to prevent cracking, so the maximum heating rate of a furnace load is limited by the size of the parts and their thermal transport coefficients.

In microwave sintering, the parts inside the microwave furnace are heated directly by absorption of microwave energy and also, in some cases, by conduction and radiation from the insulation and other fillers inside the cavity. Because of this direct coupling of microwave energy, the macroscopic thermal gradients inside the parts are reduced significantly. This leads to more uniform heating through the parts, and hence higher heating rates and shorter sintering times can be achieved.

1.2.1   Tungsten Carbide Microwave Sintering Technology

The coupling of microwave energy to a material depends on the dielectric properties of the sintering material, the geometry of the parts and the size and spatial arrangement of the load. Since hard metal is a metal-ceramic or metal-semimetal compound, the dielectric properties of the sintering parts strongly depend on the compact density of the green parts, the composition of the materials and the temperature. As green density increases, the complex permittivity, ε^*, of a material, will increase, so the microwave penetration depth into the parts will decrease,. The influence of composition and temperature are much more complex, and depend on the particular hard metal system. Table 1.1 shows the microwave penetration depth for those materials related to WC/Co

hard metal fabrication.

Table 1.1   Penetration depth of 2.45 GHz microwaves at 20°C for different materials [1]

Material	Penetration depth
Co	2.5 μm
WC	4.7 μm
WC-6%Co as sintered	4.3 μm
WC-6%Co green parts	75 mm

WC/Co hard metals can be produced either by microwave sintering of WC and Co powders or by microwave reaction sintering of W, C and Co powders; both processes are achieved in an atmospheric pressure microwave-sintering furnace.

As M. W. Porada [2] has reported for the WC/Co powders sintering process, microwave power is generated by magnetrons and typically passed into a graphite resonator, which is surrounded by thermal insulation. The resonator cavity can be heated by resistance heaters to achieve 'hot walls' and to prevent an inverse temperature gradient of the hard metal load inside the resonator. The load temperature and the microwave power are measured to allow control of the sintering process by means of a microprocessor. With such a set-up, hard metals and also cermets with high (25 wt. %) or low (4 wt. %) binder metal contents can be sintered to full density without pressure at peak temperatures which are around $50\text{-}100K$ below the conventional sintering temperature. Comparison between the microwave sintering and conventional sintering processes shows that most of the densification in microwave sintering takes place at much lower temperatures than in conventional sintering [3] and clearly below the eutectic temperature. The total sintering cycle time also decreases to 1/3 that of the conventional sintering process.

Reaction sintering of hard metals is an interesting step towards optimizing the

production methods. In this process, carburization of the tungsten powder is not carried out in a separate processing step but it is integrated into the sintering process. The compacts are shaped by the usual methods, but instead of WC and Co powders, a mixture of W, Co and C powders is used as the starting material. The exothermic carburization reaction: W + C → WC, with a reaction enthalpy of 38 kJ/mol, takes place after the lubricant is burned out of the compact, at a temperature of around 930°C. The reaction heat that evolves contributes to additional volume heating in the compact and permits a shortening of the sintering process.

Willert-Porada [4] reported that full density could be achieved by microwave reaction sintering of WC/Co at a temperature approximately 100°C lower than in conventional reaction sintering, and that hardness was improved by 10%, while many conventional process steps can also be eliminated, and hence shorten the time of the sintering process.

Since the microwave sintering time is reduced to 1/3 that of the conventional sintering process and the sintering temperature is tens of degrees lower, the microwave sintering process will give the hard metal parts remarkable improvements in microstructure and mechanical properties.

As was noted before, the coarsening rate during the last stage of sintering largely depends on the sintering temperature and sintering time. Tens of degree reduction of the sintering temperature will significantly reduce the grain size and shorter sintering time also impedes grain growth. [5] As Willert-Porada reported, the grain size of microwave sintered parts can be reduced to 1/2 or 1/3 of that produced by the conventional sintering processes. Plate-like crystals of WC can be achieved by microwave reaction-sintering of WC/Co, and the anisotropic hardness of these crystallites will help to increase the bulk material hardness and toughness. A 10% increase in hardness can normally be achieved from microwave sintering or microwave reaction sintering. This improvement of hardness gives up to 100% increase in cutting performance of the coated hard metal cutting parts sintered by microwave heating.

With the demands for higher performance tooling, the use of nano-grain and ultra-fine grain WC/Co powders continues to grow for the manufacture of tools. The major challenges in using these nano-grain WC/Co powders include the manufacture and handling of the finer powders and control of grain growth during sintering.

Several research groups have been involved in developing nano-grain WC/Co hard metal tools. Nanodyne Inc. sponsored a research program on nano-grain and ultra-fine WC/Co powder metallurgy. Their researchers [15] developed a technology using a "molecular mixing" technique to produce nanoscale grain powders. Salts of tungsten, cobalt and vanadium were dissolved and spray dried to yield flowable, dust-free particles, and then a gas phase carbothermic process was used to carburize the mixed powders. Subsequent milling processes helped to compact and distribute the pre-alloyed powders. These pre-alloy and molecular mixing techniques produced uniform and molecularly distributed nanoscale WC, Co, and VC grains in the powders. The average grain size was less than 50 nm. The powders were conventionally sintered at 1380°C. The grain size of WC-10%Co with 0.2%VC produced using the molecular mixing technique were the same as that of WC-10%Co with 0.4%VC using mechanical mixing. Also, the grain size of the WC-10%Co with 0.2%VC produced using mechanical mixing are 2-4 times larger than that of WC-Co with the same composition but using molecular mixing. As was discussed before, the lower VC component gives higher toughness to the parts. The major advantage of this technique is to reduce the component of grain growth inhibitor additives, and thereby increase the toughness of parts at the same hardness level. However, the paper reported that even better results would be obtained with Nanocarb powders, which have much smaller grains than the Microcarb powders reported here.

Sadangi [7] reported that the sintering temperature could be reduced as low as 1250°C using nanoscale WC/Co powders with vanadium inhibitor because of the decrease of the eutectic temperature with the smaller particles. This will also help to minimize grain growth, which is governed by the solution/reprecipitation mechanism. The hardness of

nanoscale WC/Co as sintered parts might be as high as 2150 HV. This work was carried out by conventional sintering techniques, but the microwave sintering technology may give much lower sintering temperature and shorter sintering time because of the different heating fundamentals. However, until now, no report can be found on the microwave sintering of nanoscale WC/Co powders.

Brookes [16] indicates in his summary of EURO PM 99, that when the WC-10%Co grain size decreased from 2.5 μm to 0.8 μm, the hardness (HV30) increased from 1400 to 1540 and flexural strength increased from 1763 MPa to 2742 MPa.

Dinesh Agrawal of Penn State University carried out research work on microwave sintering WC/Co with the cooperation of Nanodyne Inc. He indicated that microwave sintering offers great promise for sintering ultrafine WC/Co, because rapid processing tends to minimize grain growth. Clearly, there is a trend to using microwave sintering technology to replace conventional sintering and produce high performance hard metal tools with ultrafine or nanoscale grains.

1.2.2 Microwave Sintering of Silicon Nitride Overview

One ceramic that can benefit industries that require much higher cutting speed is silicon nitride. It was predicted that a quantum jump in performance would result from using silicon nitride tool bits and it has been realized. For example, in machining cast iron brake drums, the silicon nitride tooling provided 4.7 times the tool life while slicing cutting time to 25% of that possible with traditional hot-pressed ceramics. [17]

Silicon nitride, stoichiometrically expressed as Si_3N_4, has two phases: $\alpha- Si_3N_4$ and $\beta- Si_3N_4$. Needle-like $\beta- Si_3N_4$ is desired to give a much higher elastic modulus, while more $\alpha- Si_3N_4$ content increases the hardness. [18] Conventional sintering of silicon nitride requires temperatures up to 1900~2000°C and a 10 atm N_2 gas pressure; Y_2O_3 and AlN are usually added to control the phase content. The added Y_2O_3 and AlN dissolves into

the Si_3N_4 grains during sintering, which stabilizes the $\alpha-$ structure. The general formula for $\alpha-$ Si_3N_4 is given as $Y_x(Si, Al)_{12}(O,N)_{16}$. [19] High-density materials (>97% theoretical) are obtained by gas pressure sintering at >1930°C. By controlling the additives, an optimized content of $\alpha-$ Si_3N_4 and $\beta-$ Si_3N_4 can be achieved to meet the required properties.

Sherritt Inc. (subsequently MicroWear, and now Indexable) has used the microwave advantages of deep penetration and uniform heating to produce Si_3N_4 cutting tool bits. [20] The process has been developed for pressureless sintering of Si_3N_4. The sintering additive consisted of alumina and yttria. Up to 1.7 kg Si_3N_4 tool bits have been sintered uniformly at 1750°C and the final density was over 99%. Much lower peak temperature (about 200°C lower than that of the conventional sintering process) and shorter sintering time (1/2 of the conventional sintering time) prevented coarsening of the grains. The properties of microwave sintered silicon nitride are shown below:

Table 1.2   Physical properties of microwave sintered silicon nitride tool bits.

Density	3.26×10^3 kg/m^3
Hardness	94.160.1 Rockwell A
	16.7~17.5 GPa Vickers
Toughness	7.5MPa m$^{1/2}$
Phase Structure	>95% $\beta-$ Si_3N_4
Grain Size	Acicular, approximately 0.5×5 μm

Scale-up of this process to a commercial level resulted in improvements in both efficiency and productivity. The lowest energy requirement was 3.6 kWh/kg, which is only 10% of the requirement for the conventional graphite-resistance heating furnace process. Less surface degradation and more uniform microstructure than those of the conventional sintering products were observed for the microwave sintered silicon nitride,

all of which resulted in improved machining performance. By using a special applicator and "close-pack-mixed" loading design, Kiggans used microwave sintering for a silicon nitride load over 10 kg/cycle, and reported superior physical properties and mechanical performance of the sintered parts. [21]

1.3   Microwave Heating Fundamentals

1.3.1   Electromagnetic Waves

Microwaves are electromagnetic waves similar to other electromagnetic waves, such as light and X-rays, traveling through free space with the velocity of light (3×10^8 m/s) and through other media with a reduced velocity. The main differences between these kinds of waves are their frequency and wavelength. Electromagnetic waves can be focused by lenses, reflected by mirrors, reflected or made to change direction at a dielectric interface, absorbed within materials and will show interference patterns.

James Clerk Maxwell developed the classical theory of electromagnetism and demonstrated that an electromagnetic wave has an associated electric field E in the x direction and magnetic field H in the y direction. The simplest electromagnetic wave is a monochromatic, plane, linearly polarized wave in vacuum. Its intensity is

$$E_x = E_0 e^{j(\omega t - \beta z)}, \; H_y = H_0 e^{j(\omega t - \beta z)}, \text{ and } H_y = \sqrt{\frac{\varepsilon_0}{\mu_0}} E_x \qquad (1.1)$$

where E_0 and H_0 are the amplitudes of the electric and magnetic fields respectively, $\beta = \omega \sqrt{\mu_0 \varepsilon_0}$, is the phase constant, ε_0 and μ_0 are the permittivity and permeability, respectively, and ω is the frequency. All points in space being considered, the wave is travelling in a single direction, which is the positive Z direction in Fig.1.4, and at any instant the value of E is the same at all points in a plane perpendicular to this direction.

Frequency (Hz)

3×10^5 3×10^6 3×10^7 3×10^8 3×10^9 3×10^{10} 3×10^{11} 3×10^{12} 3×10^{13} 3×10^{14}

Long wave radio | AM broadcast radio | Shortwave radio | VHF TV | FM broadcast radio | Microwaves | Far Infrared | Infrared | Visible light

10^3 10^2 10 1 10^{-1} 10^{-2} 10^{-3} 10^{-4} 10^{-5} 10^{-6}

Wavelength (m)
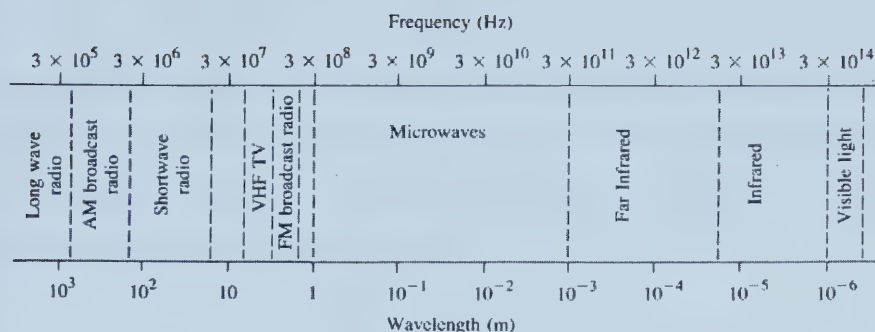
Typical Frequencies		Approximate Band Designations	
AM broadcast band	535 – 1605 kHz	L-band	1 – 2 GHz
Shortwave radio	3 – 30 MHz	S-band	2 – 4 GHz
FM broadcast band	88 – 108 MHz	C-band	4 – 8 GHz
VHF TV (2 – 4)	54 – 72 MHz	X-band	8 – 12 GHz
VHF TV (5 – 6)	76 – 88 MHz	Ku-band	12 – 18 GHz
UHF TV (7 – 13)	174 – 216 MHz	K-band	18 – 26 GHz
UHF TV (14 – 83)	470 – 890 MHz	Ka-band	26 – 40 GHz
Microwave ovens	2.45 GHz	U-band	40 – 60 GHz

Fig. 1.3 Electromagnetic spectrum from MHz to PHz (10^{15}Hz) and their applications. [22]

For a plane linearly polarized wave, the electric field strength vector E lies in one direction only. Maxwell's theory predicts that, for a plane wave, E and H must be perpendicular to each other and to the direction of propagation and hence E must be perpendicular to the Z-axis of Fig. 1.4.
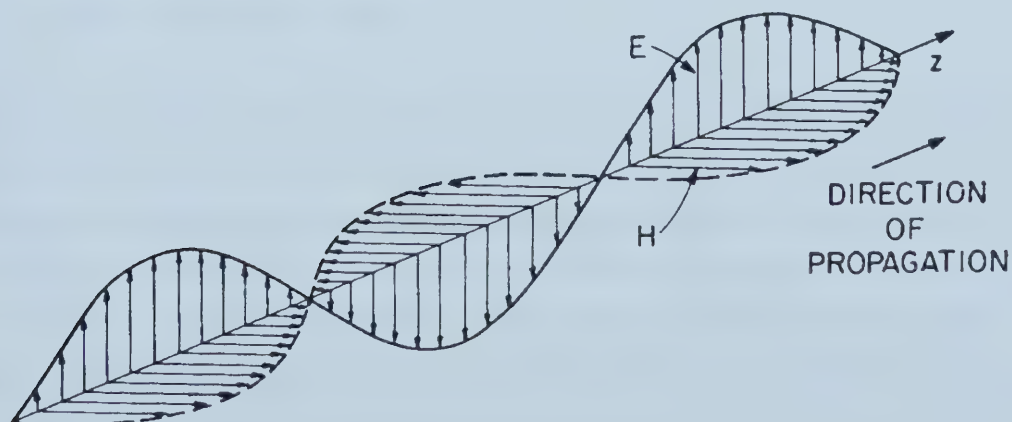
Fig. 1.4 A plane monochromatic electromagnetic wave. [23]

13

The propagation speed of electromagnetic waves traveling in vacuum or air is the same as the speed of light, $c = 3 \times 10^8 \ m/s$, while the speed of electromagnetic waves travelling through a medium is denoted by υ_p, which is related to the complex permittivity and permeability of the medium by

$$\upsilon_p = \frac{1}{\sqrt{\mu^* \varepsilon^*}}.$$ (1.2)

Wavelength, λ, is defined as the distance between two successive maxima (or minima, or any other reference points) on the wave, at a fixed instant of time. Thus,

$$\lambda = \frac{2\pi\upsilon_p}{\omega} = \frac{\upsilon_p}{f},$$ (1.3)

where ω is the frequency in radians, while f is the frequency in *Hertz*.

1.3.2   Microwave Heating Mechanisms of Solids

1.3.2.1   Phenomenological Aspects

Microwaves can be reflected, absorbed and/or transmitted by materials. Reflection and absorption require the interaction of the microwaves with the materials, and the transmission is the result of partial reflection and incomplete absorption. A microwave is not an energy generator, which gives heating itself, but an energy carrier that is manifest as heat through its interaction with materials. In other words, they cause materials to heat themselves. Materials, in their gaseous, liquid or solid state, can interact with microwaves and be heated. Some of the interaction processes involve phase transformation or composition changes, which are the result of microwave heating or microwave effects.

14

Under certain conditions, gases can be ionized by microwaves to form plasma that also can be used in materials processing.

Metals, at least in bulk form, are good conductors and excellent reflectors of microwave energy and in general are not heated significantly by microwaves. But, metal powders can absorb microwaves and be heated to high temperature. Other materials absorb or reflect microwave energy to various degrees depending on their composition, structure, temperature and the frequency of the microwaves. The microwave absorption and reflection properties of certain kinds of materials are expressed by attenuation coefficients and reflection coefficients, which are related to the dielectric constant and loss factor of the material. However, the "constants" change with temperature or frequency of the microwaves.

At room temperature, many ceramics do not absorb microwave power at 2.45 GHz sufficiently. However, their absorption can be increased by increasing the temperature, adding absorbing constituents (e.g., SiC, carbon, binders), altering their microstructure and defect structure, by changing the physical form (e.g., from bulk materials to powders) or by changing the frequency of the incident microwaves. [24] Some materials have high attenuation coefficients but high reflection coefficients as well; so most incident microwave power is reflected. In this case, microwave heating could be difficult. Hybrid microwave heating can solve this problem by either using an independent heat source such as a gas or electric furnace in combination with microwaves, or through the use of an external susceptor that couples with the microwaves. Hybrid heating can result in a more uniform temperature gradient because the external heat source minimizes surface heat losses, which occur when microwaves heat volumetrically.

The dielectric loss in a material is caused by the movement of ions or the reorientation of dipoles. The mechanisms of dielectric loss vary with the materials and applied electric fields.

1.3.2.2 Polarization and Dipolar Rotation

Some molecules are dipolar in nature; that is, they possess an asymmetric charge center such as water. Other molecules may become "induced dipoles" in an electric field. Once an electric field is present, randomly oriented dipoles in materials will be pulled into alignment. However, when the field decreases to zero, the dipoles return to their random orientation state. Once the field builds up to its opposite polarity, the dipoles will be pulled into alignment again. In a microwave field, this build up and decay of the electric field occurs at a frequency of millions of times per second. Dipoles are reoriented at high speed and driven to move or rotate in such an AC field. In a solid, atomic vibrations and dipole displacement or rotation will be converted directly into a rise in temperature. [25] In other words, microwaves cause an energy conversion from electrical field energy to stored potential energy in the material and then to stored random kinetic or thermal energy in the material. [26]

1.3.2.3 Ionic Loss Mechanism

In nonmetallic solid materials, such as ceramics and glass, the dielectric losses would be expected to be electric field dependent since we are dealing with ionic charge carriers. The presence of an electric field would cause the segregation of charge carriers of opposite sign, and prevent their recombination, while their dissociation rate, which is a thermally dependent factor, would remain constant with field strength. However, at any given temperature the concentration of ions would be expected to increase with increasing electric field strength, thereby leading to an increase in loss with the field. The presence of charges in solid insulating materials is often due to impurity contamination effects, or a 'defects' effect. In regular crystalline structures, such as those found in ceramics, the ions are normally held rigidly in the crystal lattices and are almost immobile at relatively low temperatures. But, crystal structures are not perfect, and defects always exist in crystal lattices. The most common types of defects are the *Schottky* and *Frenkel* type. In *Schottky*-type disorders, ions are missing from lattice points, hence producing vacancies,

whereas in the *Frenkel*-type disorders cations are displaced to interstitial positions producing extra charges at those spots, as delineated schematically in Fig. 1.5a and b, respectively. To maintain charge neutrality these defects always occur in pairs as shown.
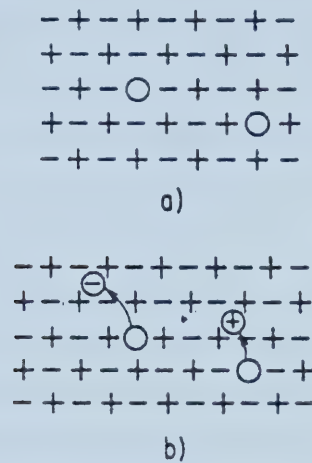
Fig. 1.5   Possible defects in crystalline dielectrics: (a) Schottky disorder and (b) Frenkel disorder. [27]

1.4   Microwave Measurement Techniques

1.4.1   Perturbation Method

The cavity perturbation method is often used for measuring the dielectric constant and loss factor in practice. It is easy to handle and can give a dynamic measurement at different temperatures. Rectangular waveguide or coaxial resonators are used as cavities for the perturbation measurement. The measurement frequencies are determined by the dimensions of the cavity and are only slightly altered as a result of the insertion of the small sample, which is to be measured. The total frequency change should be relatively small, that is to say, the insertion of the sample should not make a significant change to the electric field distribution inside the cavity. Materials with high dielectric loss can be measured if the volume of the sample is small enough. The cavity perturbation method involves the use of the following procedures:

1) Measure the unloaded Q factor, Q_0, at 3dB bandwidth and the resonant frequency f_0 of the empty cavity.

2) Place a small sample at the location in the cavity where the electric field strength is a maximum. Measure the loaded Q factor, Q_L, at 3 dB bandwidth and the resonant frequency shift Δf.

3) Calculate the dielectric constant and loss factor of the measured sample from Q_0, Q_L and Δf.

The dynamic measurement range of the perturbation method is limited by the sample material's dielectric loss tangent and the sample volume used in the measurement. Large samples with high dielectric loss tangent will exceed the dynamic measurement range, causing the Q factor to be too low to be measured and the frequency shift to be too large to satisfy the perturbation method constraints.

1.4.2   Measurement of Dielectric Constant at High Temperature

Permittivity data as a function of temperature and frequency are needed for the simulation of microwave heating systems. Data of this kind are also necessary for the selection of suitable dielectric materials for electronic applications. Furthermore, the permittivity variation can provide information on physical changes (e.g. phase changes) of a material or chemical reactions.

The cavity perturbation method can be used in both the reflection and transmission modes. These modes are employed to measure the dielectric constant at high temperature. However, heating the sample to the desired temperature, especially high temperatures up to 800°C, has proven to be very difficult using the cavity perturbation method. [28]

The sample can be heated by external means to a certain temperature before insertion into the cavity, but the actual sample temperature during the measurement is difficult to

determine this way. We can also heat the whole cavity to the desired temperature together with the sample. However, this is even more problematic because the oxidation of the materials of the measurement chamber will change the Q factor of the cavity continuously which can not be distinguished from the loaded Q_L measured in the test. In some cases, this method might be realized by using special materials or coatings to construct the cavity to eliminate the oxidation of the inner face of the cavity. Nickel and gold plate waveguide were tried to avoid the oxidation of the waveguide at high temperature. But this effort proved to be unsuccessful. Another possible solution to measure the materials' dielectric constant at high temperature is by the use of a small sample and heating it directly by a laser [28]. However, it is a very expensive approach.

1.4.3 Single Frequency Coaxial Dielectrometer [30]

W. Tinga [29] developed a Single-Frequency Coaxial Dielectrometer which focuses the microwave power in a small area and heats the sample to high temperature, and at the same time, measures the microwave properties of the sample during the microwave heating. Theoretically, all materials that can be heated by microwave can also be measured by this equipment at high temperature. However, some materials can not be heated because of their low dielectric loss factor.

In practice, the single frequency coaxial dielectrometer is often used to measure the dielectric constant and loss factor of small cylindrical samples. A voltage-controlled oscillator is used to drive a variable output power amplifier, which delivers power via a high power reflectometer into a coaxial resonator containing the sample material. The power input into the coaxial resonator can also be used to heat the sample. Because the temperature of the sample keeps changing during the measurement process, the dielectric loss of the sample also changes. And hence, the reflected power detected by the reflectometer keeps changing. The reflectometer then gives the data to calculate the new resonant frequency of the cavity at that temperature. The data obtained are also used to calculate the cavity's Q-factor by a single frequency Q-factor measurement technique. A PC control system is employed to change the voltage of the voltage-controlled oscillator,

and hence, change its frequency to the new resonant frequency of the resonator. In fact, it is a real-time control system, which provides dynamically adjusted resonant frequencies. It is important to limit the shift of the resonant frequency so as not to exceed the dynamic range of the perturbation method. The frequency used to measure the Q-factor at a certain time is that corresponding to the maximum return loss which indicates resonance. Similar to the perturbation method, we can also get Q factor and frequency shift, and thus the dielectric constant and loss factor of the material at a certain temperature can be calculated. A series of loss factors calculated using this system could give a profile of the material's dielectric loss factor versus temperature.

As a perturbation method, the single frequency dielectrometer is constrained by a maximum allowed frequency shift, which is proportional to the value of the dielectric constant. In practice, the tungsten carbide sample has a very high loss factor and even a small sample is out of the perturbation measurement dynamic range. On the other hand, the silicon nitride sample has a very low loss factor at low temperature. It is hard to heat the silicon nitride samples from room temperature with the available microwave power. Unfortunately, the single frequency coaxial dielectrometer has proven unsuitable for the measurement of the dielectric properties at high temperatures of both materials of interest.

1.4.4 Attenuation Method

Fortunately, all that we need to simulate the microwave absorption and reflection situation in the real process is what per cent input power is reflected or absorbed by the various materials involved in the furnace at different temperatures. The front face reflection and the attenuation constant can be calculated from the loss factor and the dielectric constant of the samples or, we can measure the front face reflection and the attenuation in dB scale directly by using a reflectometer and the attenuation method. It is this latter method which was employed in this thesis work.

The samples were mounted in a rectangular waveguide, which was surrounded with

several resistance heaters. The input microwave signals were reflected back or transmitted through the samples. The return loss along with the transmission loss of the samples were recorded using a scalar network analyzer. The resistance heater was used to heat the waveguide and the sample load to the required temperature. As we already know, the percentage of the reflected power can be calculated directly from the return loss and the transmitted power through the sample can be calculated from the transmission loss.

CHAPTER 2   MICROWAVE ATTENUATION MEASUREMENT OF THE ABSORPTION PROPERTIES OF THE SUSCEPTOR MATERIAL

In order to model the heating process of the microwave-sintering furnace at Indexable Tool Co., the microwave absorption properties of the materials involved in the process must be known. One key technique used to sinter ceramics, ceramic composites and metal powders is to use a special mixture of susceptor materials around the work piece. The susceptor bed includes granules of a major amount of a microwave susceptor material, and a minor amount of a refractory parting agent, either dispersed in the susceptor material, or as a coating on the susceptor material. [32] The work introduced in this chapter focuses on the microwave measurement of the susceptor materials' absorption properties.

Several ways were tried to measure the dielectric properties or microwave power absorption properties of the susceptor mixture. However, the dielectric constant and loss factor are very difficult to measure directly by the perturbation method. The single frequency dielectrometer was used to measure the dielectric constant and loss factor of the susceptor material. [34] Because of the large size of the susceptor particles, there are big variations between the data recorded in different tests. It is difficult to find a reliable dielectric constant versus temperature and loss factor versus temperature curves from those measurements which we need to simulate the real process. However, although the attenuation method measurement cannot give the dielectric constants or loss factors of the samples, it can measure the attenuation coefficients at different temperatures, which also allows calculation of the microwave absorption properties of the materials. Hence, the attenuation method is employed to measure the microwave absorption properties of the susceptor mixture.

2.1 Experimental Setup and Sample Preparation.

In order to understand the microwave absorption properties of the material, an experimental system, which combined the microwave power measurement system and a

resistance heating system has been used. The samples were heated not by the microwaves but by the resistance heaters. Microwave signals are introduced into the waveguide containing the sample load. Transmitted signals as well as reflected signals are detected and recorded by the microwave measurement system. The input microwave power is of the order of mW, so there is no significant microwave heat generated in the materials. The experimental setup is shown in Fig 2.1 and Fig 2.2.
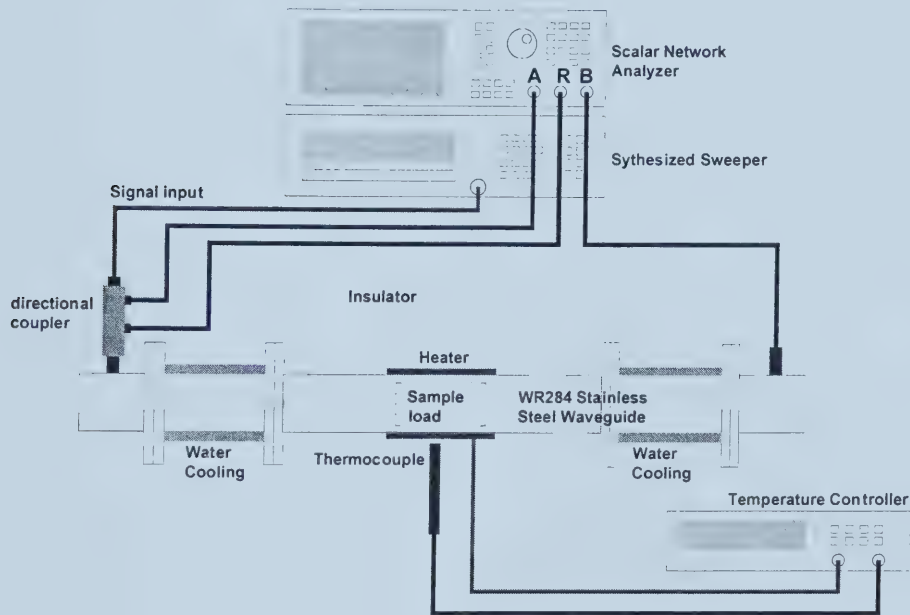
Fig. 2.1 Attenuation test block diagram.

The microwave signals were generated by a HEWLETT PACKARD 83752A Synthesized Sweeper set for a bandwidth of 2.3 GHz to 4.0 GHz. The microwave input power, reflected power and transmitted power were detected by a HEWLETT PACKARD 11664 Detector 0.01~18 GHz. A HEWLETT PACKARD 8757D Scalar Network Analyzer was used to analyze and record the data. The attenuation data in dB were recorded at a certain frequency. Samples were mounted in a 2.45 GHz stainless steel waveguide as shown in Fig.2.3. The resistance heaters were outside of the waveguide.

Mica windows were used at the ends of the waveguide to limit heat convection and water-cooling coils outside of the waveguide were used to cool the ends of the waveguide to provide an acceptable temperature condition for the detectors.
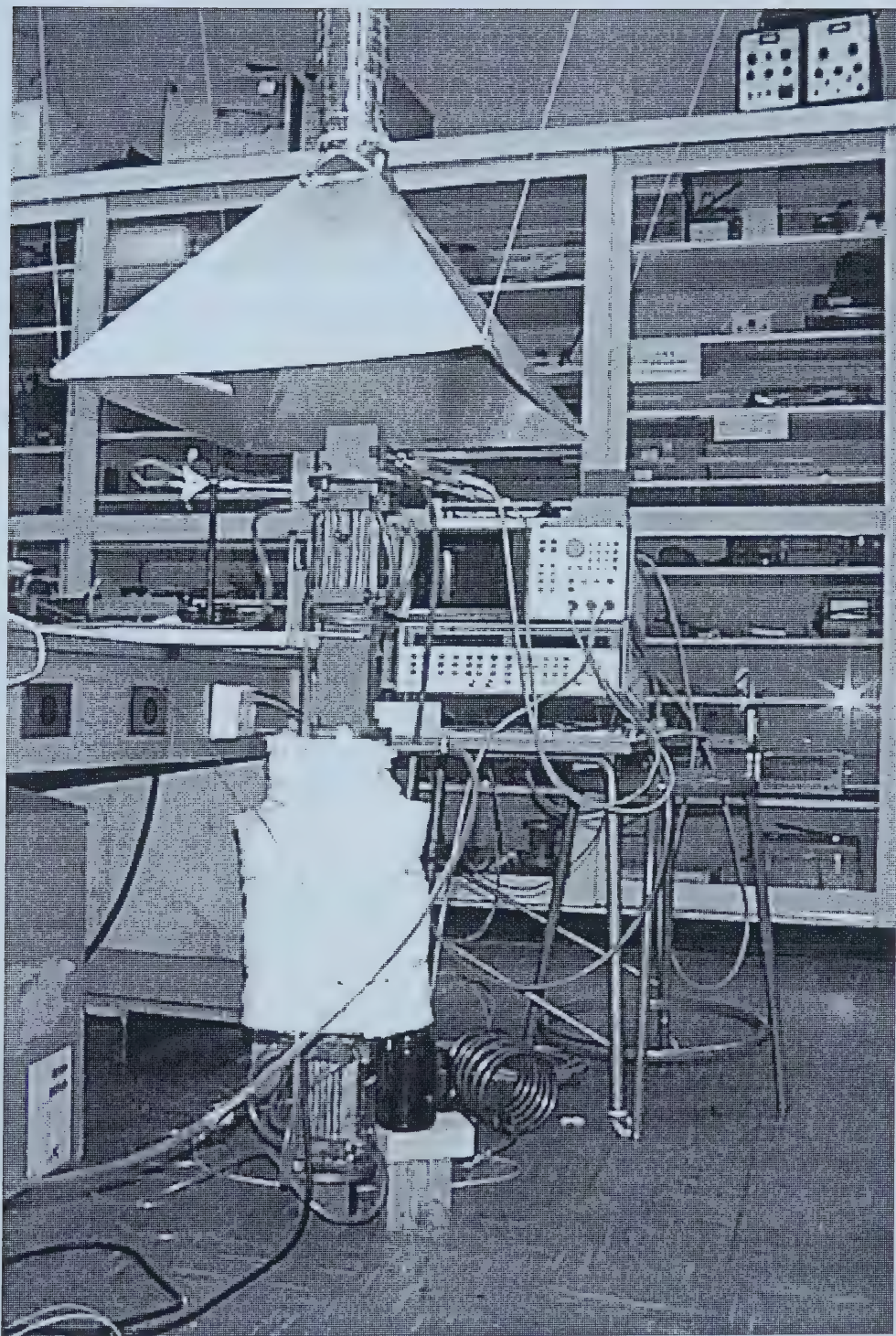
Fig. 2.2 Experimental Attenuation test setup

The hot area of the waveguide was surrounded by insulation. The temperatures at the center of the heating region were detected by a thermocouple mounted externally to the waveguide. An MPI-VT4801 PID temperature controller was used to control the heating process. Data were recorded every 100ºC, and it usually took one hour to get a uniform temperature in the heated region of the waveguide. In the comparison tests, nitrogen gas flow was directed into the waveguide through stainless steel pipes at the end of the hot area.
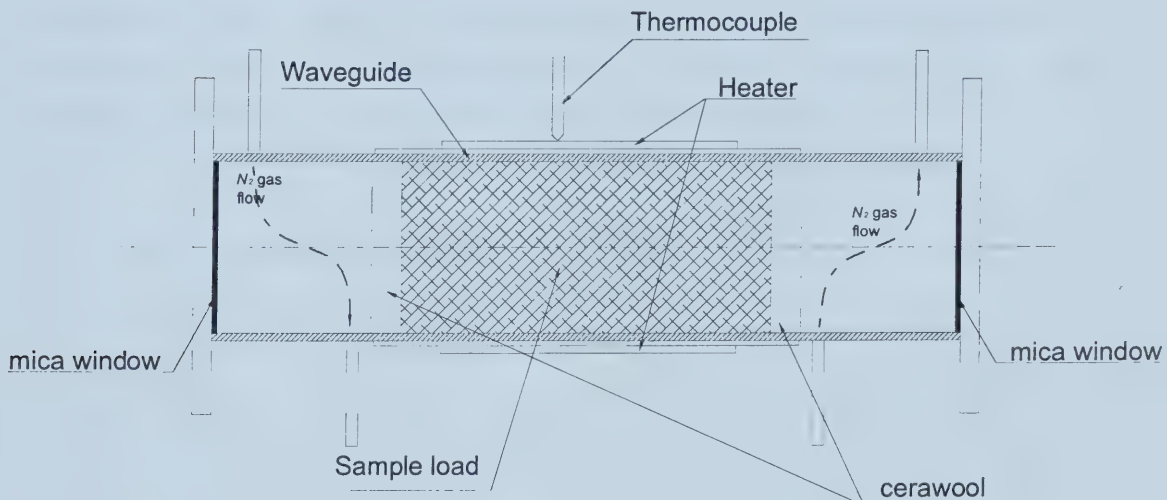
Fig. 2.3 Sample load in the waveguide sample mount.

2.2 Results and Discussion

2.2.1 Transmission Test on the Susceptor Mixture Materials in Air

The attenuation properties of the susceptor mixture materials versus temperature (from 20°C to 800°C) in air (without any protecting gas flow) have been measured and the results are shown in Fig 2.4.

The attenuation increased from 20°C to 500°C then leveled off and began to decrease as the temperature increased further. The attenuation after cooling the sample down to room temperature was less than that before the heating process. The reason for this was believed to be oxidation of one of the constituents in the susceptor. The longer we waited at a given temperature to record the data, the greater the change. Since the peak temperature was much lower than that in the production process, the oxidation change was not complete after the test. Based on the data for the susceptor without the proprietary oxidizable constituent recorded by Tinga in earlier tests, we determined that a typical one inch thick cylindrical susceptor without oxidizable constituent has an attenuation of about 0.02 dB, which means the susceptor is nearly transparent to microwaves at room temperature. Obviously, the oxidizable constituent plays a very important role in the microwave power absorption of this susceptor.
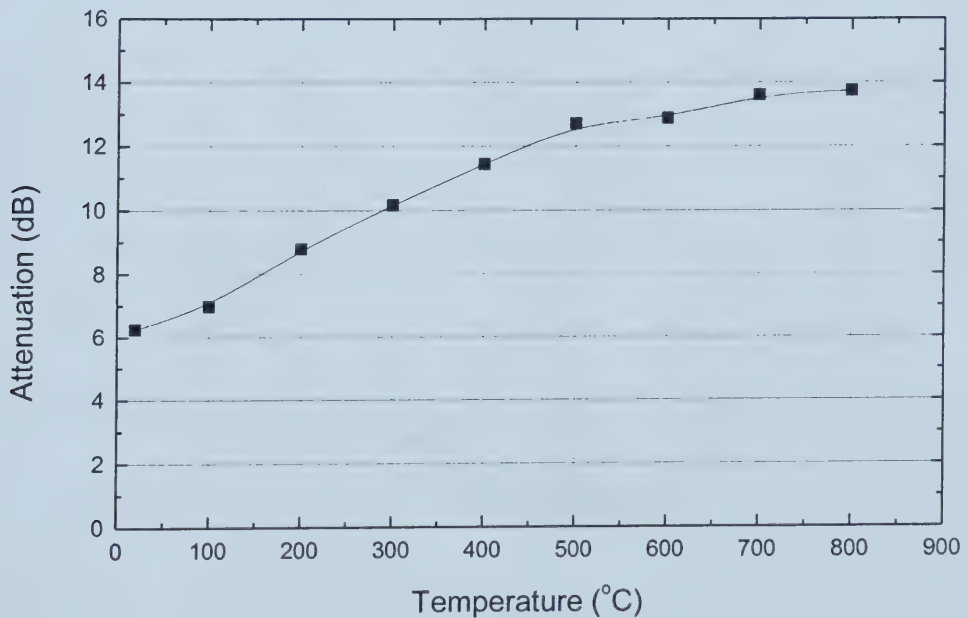
Fig. 2.4 Attenuation through a bed of susceptor mixture measured in WR284 Stainless steel waveguide at 3.00 GHz in air. Sample weight: 278 g, length 190 mm.

2.2.2　Transmission Tests on the Susceptor Mixture With Protecting Gas Flow:

Nitrogen gas was used to surround the sample in the second test of the attenuation of the susceptor mixture versus temperature. Since only a very small amount of the oxidizable ingredient was burned out during this test, the attenuation increased more linearly and reached much higher values than those obtained from the tests without any gas protection as shown in Fig. 2.5. The reflection signal in both measurements was about -20 dB, which is below 2% and can be neglected.
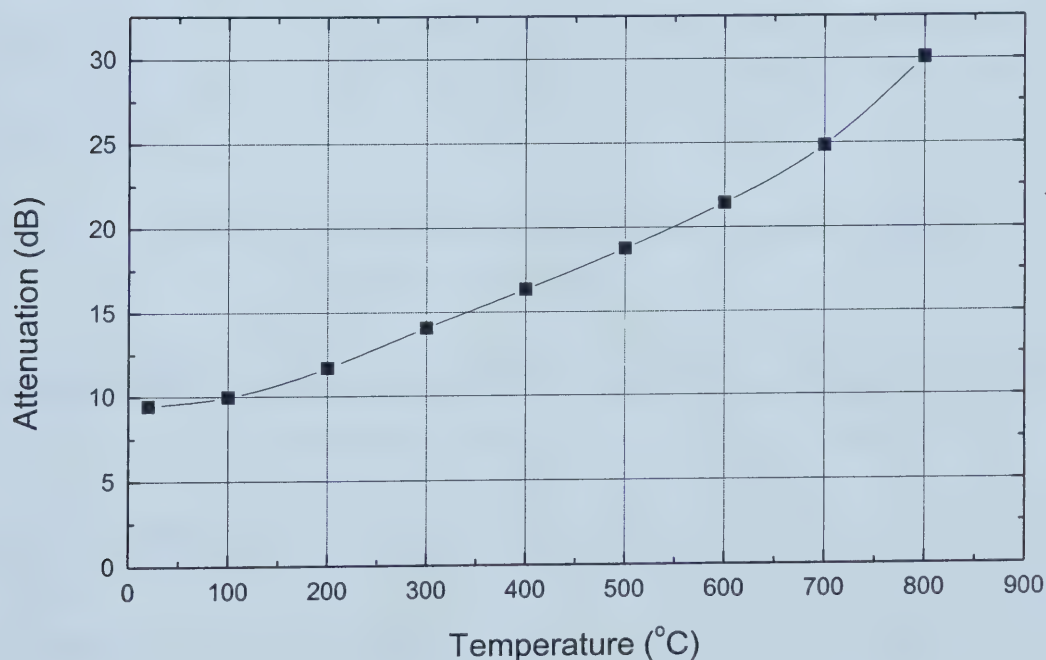
Fig. 2.5 Attenuation through a bed of susceptor mixture measured in WR284 stainless steel waveguide at 3.00 GHz with a protecting N_2 gas flow. Sample weight: 289 g, length: 195 mm.

But an interesting thing is that after the sample cooled down to room temperature, the attenuation remained at a very high value (just a bit lower than that at 800°C) which means some permanent change in the material occurred during the process. To pursue this further, argon protecting gas was used in a comparison test instead of N_2. The results are listed in Table 2.1. Obviously, it is not a chemical reaction between the input gas and the oxidizable agent that causes the permanent change. Tinga's (ref. 33) perturbation method was used to measure the dielectric constant and loss factor of the susceptor samples. Susceptor mixture samples were placed in a small quartz tube and capped with a cork which made the tube airtight. The dielectric constant and loss factor of the sample were then measured at room temperature, in the red-hot state (about 800°C) and at room temperature after cooling. The result was similar to that obtained using the attenuation method, that is, the loss factor of the treated sample after heating and cooling was much higher than that of the green one. Obviously, there is a physical change occurring during the heating process.

Table 2.1   Comparison of the attenuation of susceptor mixture samples in different heating environments.

Susceptor mixture	Attenuation at 20°C before heating (dB)	Attenuation at 800°C (dB)	Attenuation at 20°C after cool down (dB)
No protecting gas flow	-9.59	-12.95	-8.27
N_2 gas flow	-9.47	-30.07	-25.93
Ar gas flow	-9.59	-31.90	-26.72

2.2.3   Resistance Test of Susceptor Mixture Samples.

In an attempt to identify the cause of the attenuation change, a resistance test system was constructed as shown in Fig.2.6. Susceptor mixture samples were placed inside a 150

mm long, 5 mm ID quartz tube which was open at both ends. Steel wool was used to fill the ends of the tube in contact with the samples. Ohmmeter probes were connected to the steel wool and the measurement range was set from 0.1 to 1000 Ω.
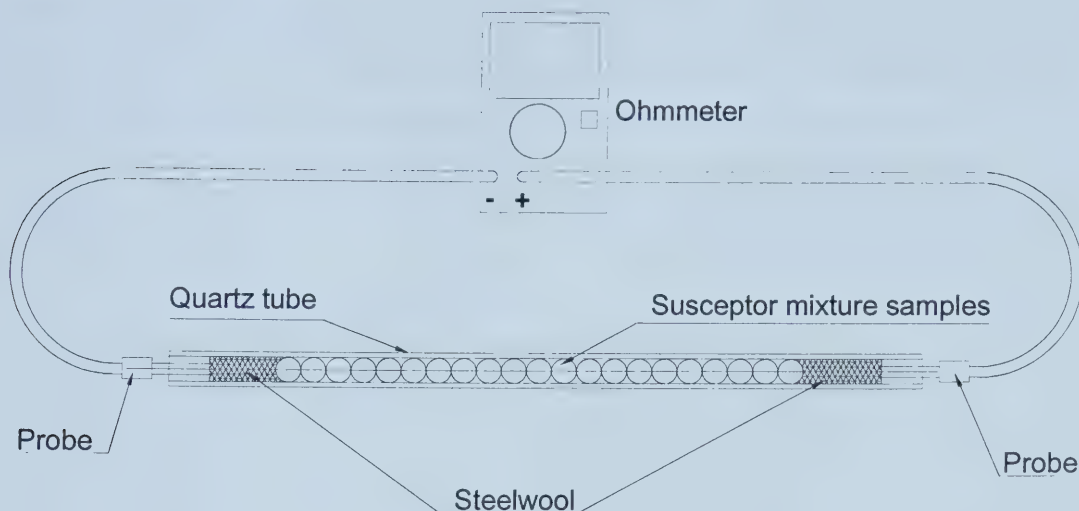
Fig. 2.6 Resistivity test system for susceptor mixture samples.

Data were recorded for the three measurements shown in Table 2.2. The results obviously show a marked change of the resistance between the green samples and the samples after heating.

Table 2.2   Results of the resistivity test of the susceptor mixture

States	Resistance (Ω)	Comments
Before heating	240±10	Green samples
Hot	40±5	Red-hot (~600°C)
After heating	55±5	Cooled to 20°C

Microwave attenuation measurements on the same kind of material show the same trends: heated samples show a much higher loss factor than the virgin samples due to the significant reduction of the resistance. There must be a permanent physical change in the susceptor materials. This change was not readily detected under a microscope possibly because the changes are no longer apparent after the sample is removed from the tubes. It is probable that the oxidizable ingredient powder consolidetes into a more conductive matrix at high temperature causing the mixture's resistance to drop significantly.

CHAPTER 3   MICROWAVE ATTENUATION MEASUREMENT OF CERAMIC AND HARD METAL TOOL BITS

3.1 Microwave Attenuation Measurement of Tungsten Carbide/Cobalt Green Parts.

To measure the microwave attenuation of tungsten carbide/cobalt green parts, the attenuation method measurement system outlined in Chapter 1 was used. The samples were mounted in the heating region of the waveguide. There was a 1 to 3 mm space between the edge of the samples and the walls of the waveguide, which would produce measurement errors below 1% and could be neglected. (Fig. 3.1)

All tungsten carbide/cobalt samples were prepared by the Indexable Cutting Tools. They were Newcomers N21 WC powder with 6%Co, pressed to a green density of 3950 kg/m^3 in a 12 ton press. The individual part size was 16.5 mm×16.5 mm×11.5 mm.

An attempt to measure attenuation using the attenuation method through several layers of WC/Co green parts with 5 mm spacing between each part was rather unsuccessful. The attenuation was not constant with frequency as a result of the interface interference patterns caused by multiple reflections. The only way to avoid it was to use one or several layers of close-packed green parts to eliminate the multiple reflections. However, tungsten carbide/cobalt is a kind of metal/semi-metal mixture, which has large reflection and attenuation coefficients. Hence one layer (16.5 mm thick) of sample in the waveguide was enough to give sufficient attenuation values.

The measured attenuation versus temperature through one layer (16.5 mm thickness) of WC/Co green parts at 2.45 GHz and 2.63 GHz is shown in Fig. 3.2. Nitrogen gas flow was introduced to simulate the real process environment. The variation of attenuation with temperature through the WC/Co green parts was relatively small (<2dB). In other

words, the power absorption of WC/Co green parts was not sensitive to temperature.
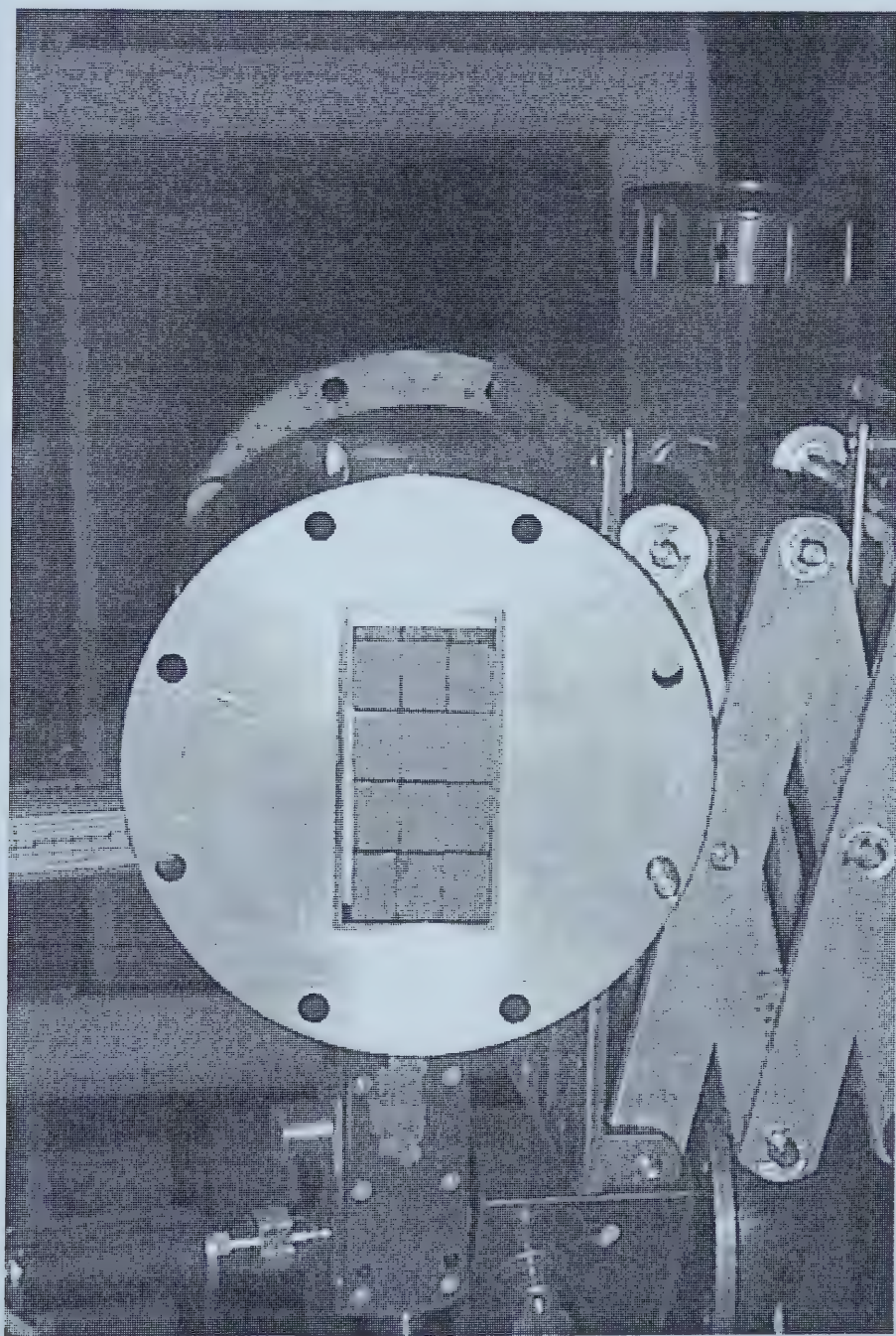
Fig. 3.1   Sample arrangement in the waveguide.
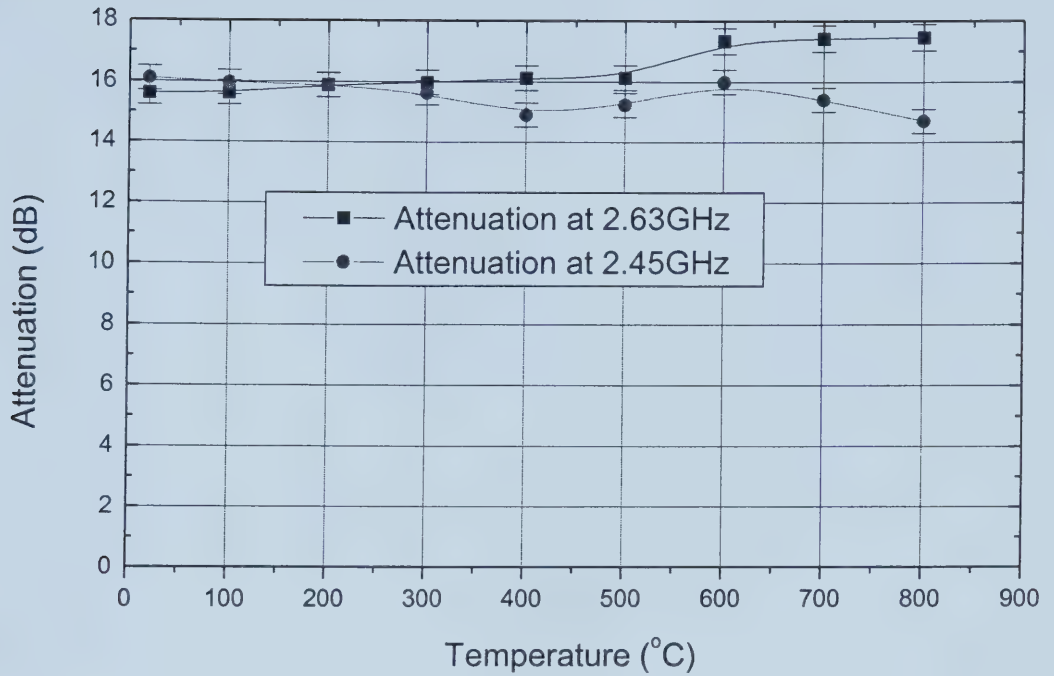
Fig. 3.2 Attenuation through one layer (16.5 mm thickness) of WC/Co green parts versus temperature at 2.45 GHz and 2.63 GHz (N$_2$ gas flow). Dewaxing occurred during the heating.

During this measurement, the return loss is quite low and cannot be neglected. The return loss is also sensitive to frequency. The return losses at 2.63 GHz were much higher than that at 2.45 GHz (Fig. 3.3). At higher temperature, the return loss will decrease which means more power will be reflected from the samples' front face. Because of the low return loss, an extra correction to the attenuation or transmission loss data must be applied before using the data in the model to be described later.
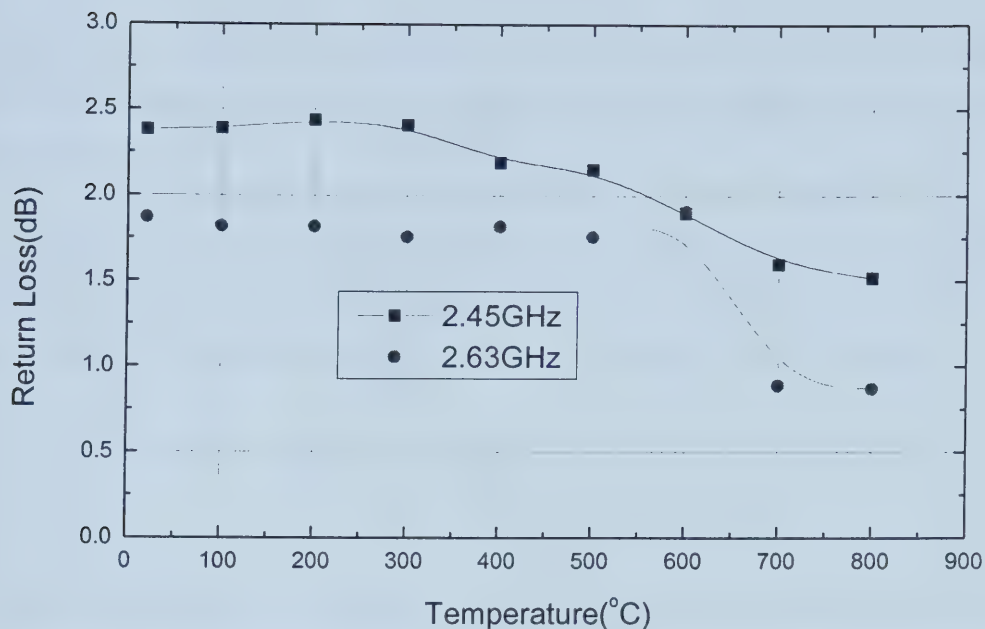
Fig. 3.3 Return loss of one layer (16.5 mm thickness) WC/Co green parts versus temperature at 2.45 GHz and 2.63 GHz (N_2 gas flow). Dewaxing occurred during the heating.

3.2 Microwave Property Measurement of Silicon Nitride Green Parts

3.2.1 Dielectric Constant Measurement of Si_3N_4 Green Parts at Room Temperature Using a Swept Frequency Technique

The reflection coefficient of a material can be calculated from the complex dielectric constant of this material, ε, using

$$r_{sa} = r_{as} = \frac{\sqrt{1-p} - \sqrt{\varepsilon - p}}{\sqrt{1-p} + \sqrt{\varepsilon - p}} \tag{3.1}$$

where r_{sa} is the reflection coefficient from the sample to air and r_{as} is the reflection coefficient from air to the sample. p denotes the square of the waveguide cutoff frequency to signal frequency ratio. [34]

Since the loss factor of Si_3N_4 at low temperature is negligibly small, the complex dielectric constant can be mainly represented by its real part. In the swept frequency measurement, p is also small enough to be ignored. Hence, Eq. 3.1 can be rewritten as

$$r_{sa} = r_{as} = \frac{1 - \sqrt{\varepsilon'}}{1 + \sqrt{\varepsilon'}} \tag{3.2}$$

There are a number of methods that could be used to do this measurement, but the swept frequency measurement technique is one of the easiest, which can provide reliable results.

3.2.1.1   Fundamentals

The swept frequency technique used for dielectric constant measurement was first developed by Tinga and Edwards [34] in 1968. However, the basic idea and theory used today are the same and the only difference is that we are using a scalar network analyzer, which can measure the return loss and show it directly on the monitor.

The experimental apparatus is set up as shown in Fig. 3.4 and Fig. 3.5. The sweeper generates the microwave signal incident to the sample, which will be partially reflected and partially transmitted. If the entire reflected signal is detected and displayed on the network analyzer monitor in the frequency domain, a characteristic interference pattern results. This pattern contains all the information we need to calculate the dielectric constant of the material we are measuring.
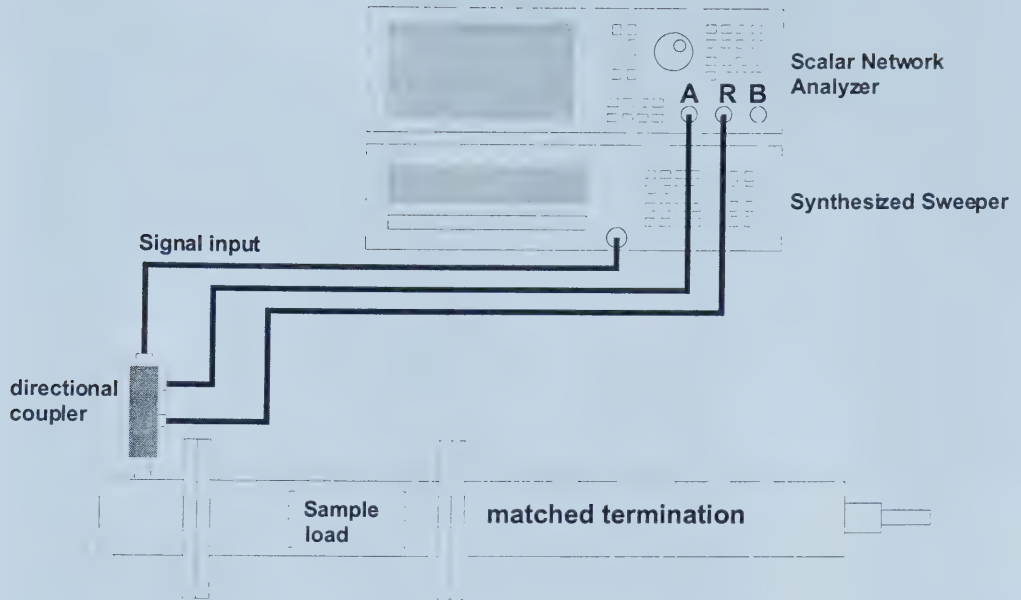
Fig. 3.4 Block diagram of the swept frequency measurement setup

Fig. 3.6 shows a diagram representing the physical system we are analyzing, where r_1, r_2, $-r_1$ and $-r_2$ are the interface reflections at the sample front face 1 or back face 2, respectively, γ is the propagation constant and l is the sample length. Assume the reflection of the termination, R_3, is negligibly small, and that the input signal is only reflected at the front and back face of the sample. The electrical length of the sample is varied with the swept frequency signal and an interference pattern is formed.
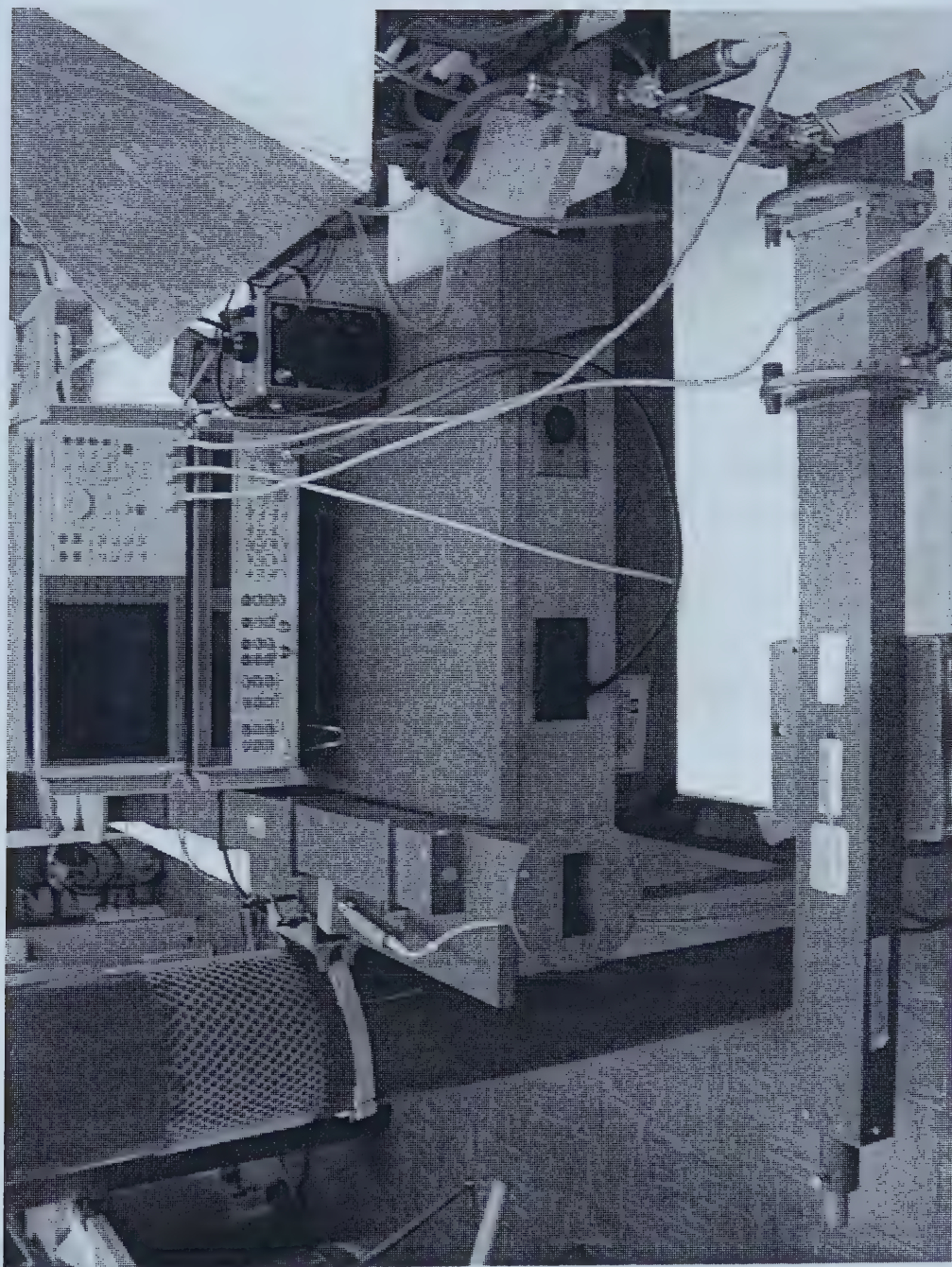
Fig. 3.5 Experimental apparatus for the swept frequency measurement
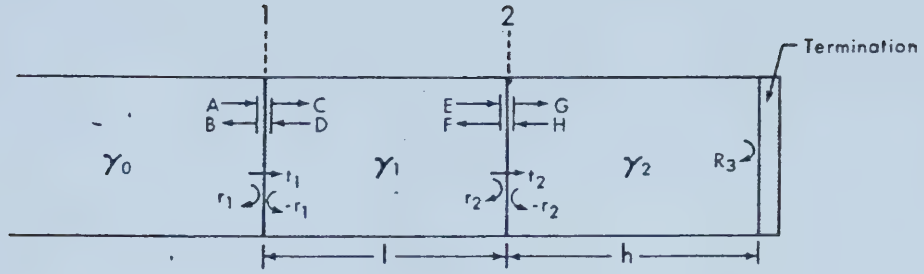
Fig. 3.6 Physical interface system to be analyzed [34].

Once the characteristic pattern is obtained from the reflection measurement, we can calculate the dielectric constant directly from the data. Using the formulae from Tinga et al. [34], we have:

$$\varepsilon' = \frac{1}{2} E \left[1 + \sqrt{\left(1 - \frac{4p}{E} \right)} \right],$$ (3.1)

where p is given by

$$p = (f_1 p_1 + f_2 p_2)/(f_1 + f_2),$$ (3.2)

where f_1 and f_2 are the adjacent frequencies at maxima or minima and E is defined as:

$$E = (c/2l\Delta f)^2,$$ (3.3)

where c is the velocity of light in free space, l is the sample length, Δf is the frequency difference between two adjacent maxima or minima, and p is the geometric mean value of p_1 and p_2, with p_1 and p_2 given by:

39

$$p_1 = (f_c / f_1)^2$$

$$p_2 = (f_c / f_2)^2, \tag{3.4}$$

where f_c is the cutoff frequency of the waveguide.

3.2.1.2 Measurement Procedure

For waveguide or coaxial tests, the equipment was set up as shown in Fig. 3.5. The waveguide is filled with samples and the length of the samples is measured. The matched load should be connected directly to the sample containing waveguide. The frequency band of the sweep is set from 2.6 GHz to 4 GHz. Longer samples will give more interference maxima or minima. The best resolution on the monitor and record the interference frequency at adjacent well-defined maxima or minima points has been chosen.

The Si_3N_4 green parts are compressed to square bits with dimensions of 16.5 $mm \times 16.5\ mm \times 11\ mm$ and a density of 1840 kg/m^3. The samples were mounted to fill the waveguide and the size of the samples is 33 $mm \times 69\ mm \times 120\ mm$. There were 1 mm gaps on the narrow dimension of the waveguide between samples and the upper wall of the waveguide and 3 mm gaps on the wide dimension. This incompleted fill produced some error, which is discussed in the section on measurement errors.

The tests were run only at room temperature. High temperature tests can also be arranged using a heater and a temperature control system.

3.2.1.3 Results and Calculation


```
CH1:   A/R              -23. 50  dB
  5. 0  dB/     REF        0. 00  dB
```

> CRSR   -23. 50 dB
> 2. 92550 GHz

STRT 2. 60000 GHz   CRSR 2. 92550 GHz   STOP 4. 00000 GHz
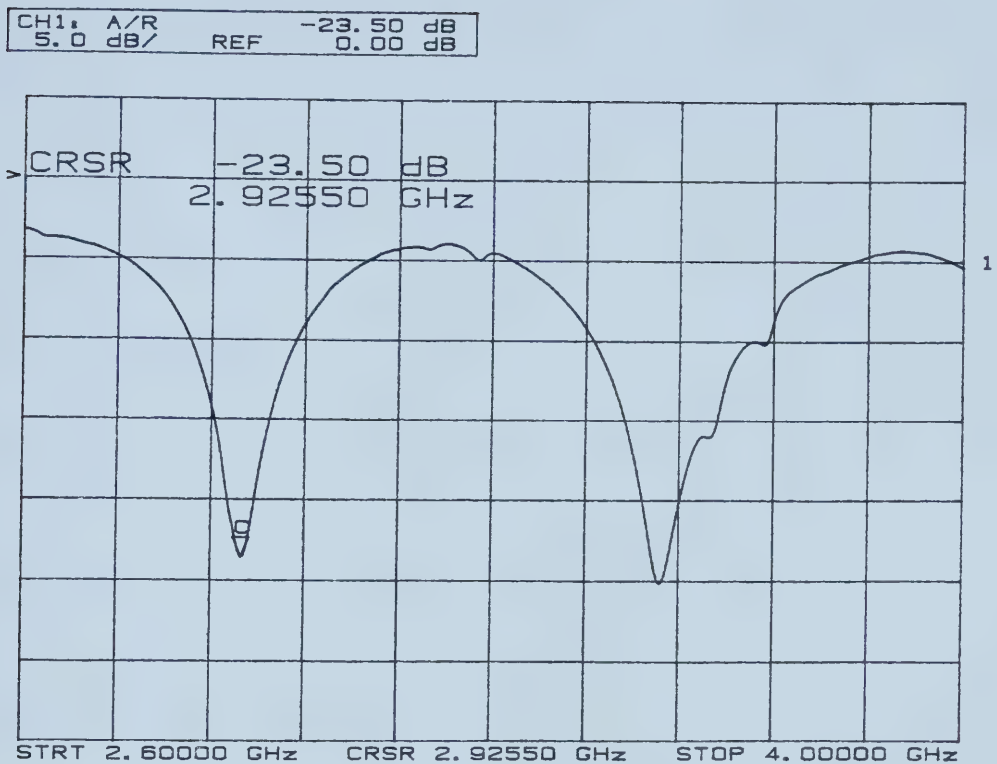
Fig. 3.7 Characteristic pattern of Si_3N_4 green parts using the swept frequency technique at room temperature in the WR284 waveguide.

The characteristic pattern of Si_3N_4 at room temperature is shown in Fig. 3.7. From this experiment, the following data are extracted.

$$f_1 = 2.925 \; GHz$$

$$f_2 = 3.552 \; GHz$$

$$l = 120 \; mm$$

$$f_c = 2.078 \; GHz$$

$$c = 3.0 \times 10^{11} \; mm/s$$

$$\Delta f = f_2 - f_1 = 3.552 - 2.925 = 0.627 \; GHz$$

$$p_1 = (f_c / f_1)^2 = (2.078 / 2.925)^2 = 0.505$$

$$p_2 = (f_c / f_2)^2 = (2.078 / 3.552)^2 = 0.342$$

$$p = (f_1 p_1 + f_2 p_2)/(f_1 + f_2) = 0.415$$

$$E = (c / 2l\Delta f)^2 = \left(30 \times 10^{10} \Big/ 2 \times 12 \times 0.627 \times 10^9 \right)^2 = 3.97$$

$$\varepsilon' = \frac{1}{2} E \left[1 + \sqrt{\left(1 - \frac{4p}{E} \right)} \right] = 3.5$$

3.2.1.4 Measurement Errors

A. Incomplete sample fill error

Since the waveguide is not completely filled with Si₃N₄ green parts, the measured value of the dielectric constant will be less than the true value. The true value of the dielectric constant is given by: [35]

$$\varepsilon'_{true} = \left(\varepsilon'_{meas} - 1\right)\left(b/b - c\right) + 1,$$ (3.5)

where b is the narrow waveguide dimension, c is the gap between samples and the wall of the waveguide.

Putting the numbers in ($b = 34mm$, $c = 3mm$), we have:

$$\varepsilon'_{true} = \left(\varepsilon'_{meas} - 1\right)\left(b/b - c\right) + 1 = 3.57$$

$$Error\% = -2\%$$

B. Summary of Experimental Errors

All the other errors caused by frequency measurement, length measurement and systematic errors are listed in Table.3.1.

Table 3.1   Summary of experimental errors for the dielectric constant of Si₃N₄ at about 3 GHz and room temperature.

	Incomplete fill error	Length measurement error $\Delta l = \pm 25\ mm$	Frequency measurement error $\Delta f = \pm 0.001\ GHz$	Theoretical systematic error	Total measurement error
$\Delta\varepsilon'$	-2%	<±1%	<±1%	<<0.1%	-4%~+2%

3.2.2   Attenuation Measurement on Si₃N₄ Green Parts

The microwave attenuation measurement of Si_3N_4 green parts used the same transmission measurement method as was used for the WC/Co samples. Because of the much lower transmission loss of Si_3N_4 green parts, the sample loads used were much longer than those for the WC/Co samples.

The silicon nitride samples were prepared by the Indexable Cutting Tools. Blend 43SDP, Lot_922 powder was used, and pressed at 1810 kg/m³ to a green density using a 12-ton press into SNR 45's. The sample size was 16.5 mm×16.5 mm×11.5 mm.

Figures 3.8, and 3.9 show the attenuation of 5-layers (82.5 mm total thickness) of close-packed Si_3N_4 green parts at temperatures up to 800°C. During the first heating cycle, the green parts has been dewaxed giving rise to a highly nonlinear attenuation versus temperature curve. After cooling the parts to room temperature, they are heated and measured a second time. The resulting attenuation versus temperature curve shown in Fig. 3.9 is now nearly linear since the parts have been dewaxed. Above 200°C, the wax, which was used as a lubricant in pressing the samples, will be evaporated. We call this the dewaxing process. When the wax evaporates from the samples, pores were left in the samples, the loss of the waxy component causes the decrease of attenuation in the green parts during the heating process. With an increase in temperature, all the wax evaporated or is converted into solid state carbon remaining in the samples; and the increase of the attenuation of samples became more linear. As can be seen in Fig. 3.8, the attenuation increases very rapidly after 600°C. Silicon nitride is a typical ceramic, which can not absorb much microwave energy at low temperatures but becomes a good microwave absorber at high temperature. The results are not sensitive to the microwave frequencies.

The experimental conditions for each test are listed in Table 3.2. Since there is a retaining ring and mica window inside the waveguide in the first measurement (curve A in Figure 3.8, and 3.9), the airflow was blocked and the dewaxing process was not

complete. Wax remaining in the samples was decomposed into carbon and H_2 gas, which significantly increased the attenuation of the samples. When the retaining ring and mica windows were removed, it left many (10) screw holes open, which allowed a greater wax removal rate through the gas outlet and holes. During measurement B the dwell time at 500°C was two hours which allowed for more complete dewaxing; hence less carbon remained and the data were more comparable to the commercial process since the samples are completely dewaxed in that process.
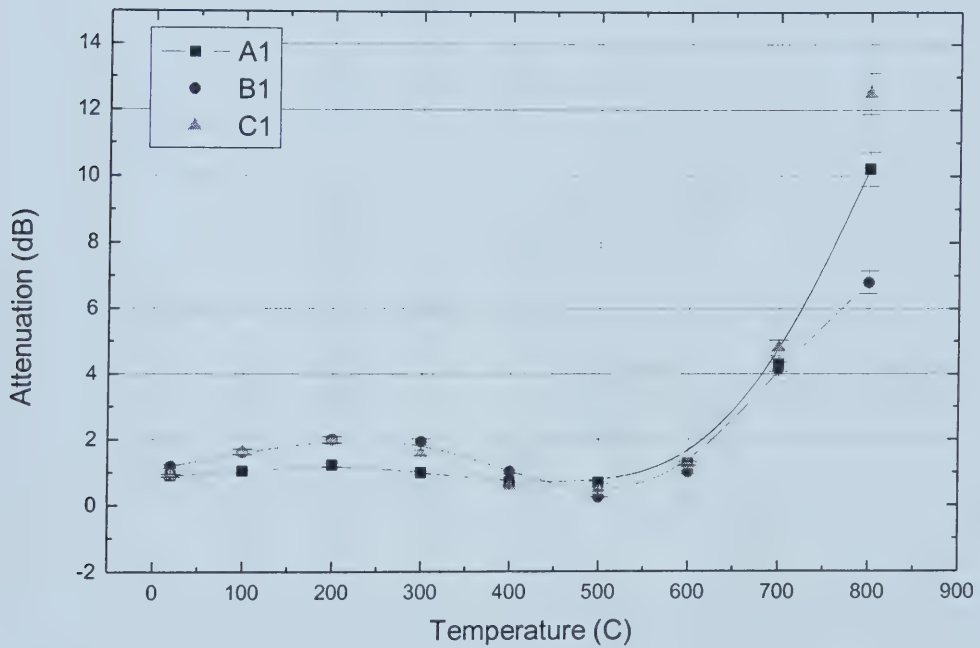
Fig. 3.8 Microwave power attenuation though 5 layers (82.5 mm thick) of Si_3N_4 green parts. First heating cycle, dewaxing occurred during this process from 200°C to 600°C. A, B and C stand for 3 different measurement rounds. The parameters of each measurement are shown in Table 3.2.

Table 3.2   Experiment parameters for different attenuation measurement of Si_3N_4.

Round	Experiment parameters	Frequency
A	Vertical (with metal retaining ring inside the waveguide); N_2 gas flow; no attenuator.	2.636 GHz
B	Horizontal (no metal holder inside the waveguide); N_2 gas flow; 6.3 dB attenuator at one end (power out) of the waveguide. Dwell at 500°C for 2 hours.	3.36 GHz
C	Same as round B, without the dwell time at 500°C.	3.36 GHz
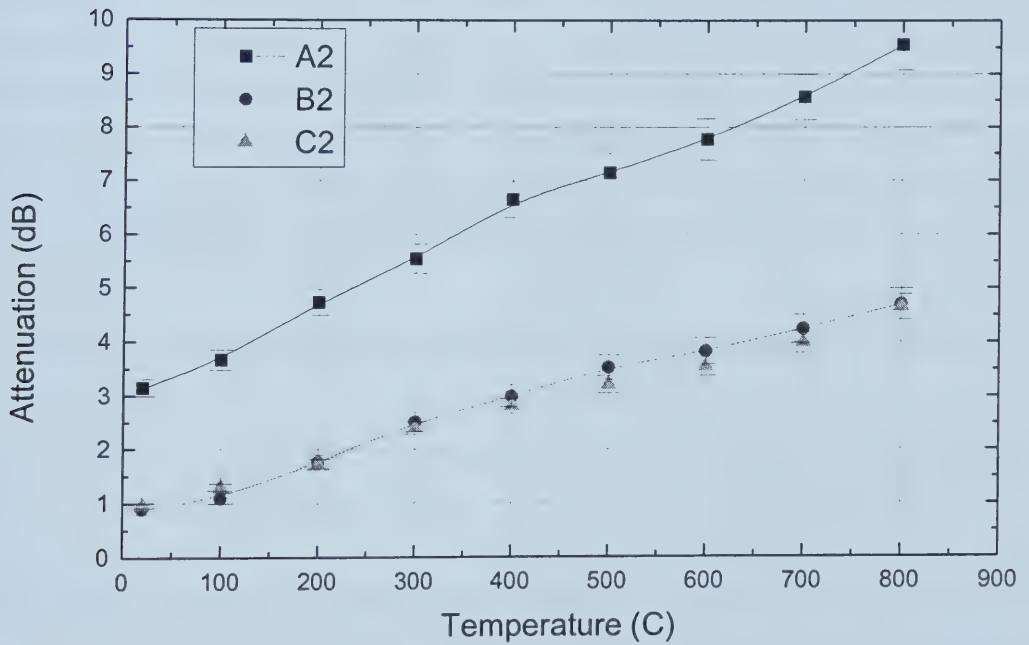
Fig. 3.9 Microwave power attenuation though 5 layers (82.5 mm thickness) of Si_3N_4 green parts. Second heating cycle. A, B and C stand for 3 different measurement rounds and their parameters are shown in Table 3.2.

CHAPTER 4   MICROWAVE SINTERING PROCESS MODEL

4.1   Overview of the Modelling Approach

Considerable work has been done in modelling the microwave sintering of ceramics processes, such as sintering of alumina [36][37], ZnO [38], SiC [39], ZrO$_2$ [40] and Si$_3$N$_4$ [41]. However, there is no report on modelling of the tungsten carbide microwave sintering process.

Models are used to predict heating process parameters such as temperature at a certain point in the sintering cavity and the heating rate of the materials. Whenever the experimental data can be matched by the model calculations, the model is verified and can be used to calculate other similar situations for microwave sintering of the material. There are several ways to do the modelling; however, all of them are based on the general concepts of microwave heating and on heat generation and heat transfer concepts. Tinga [42] has summarized the modelling fundamentals for the microwave heating of materials which is the starting point for the microwave process model.

Assume in an isotropic rigid solid, the heating rate of the material can be given by:

$$\frac{dT}{dt} = \frac{Q}{C_p \rho} \quad (°K/s) \tag{4.1}$$

where Q is the internal heat generated by the absorption of power, P, and $Q = dP/dv$ in W/m^3, where v is the volume in m^3, C_p is the molar heat capacity in $J/kg.K$, ρ is the mass density in kg/m^3, T is the temperature in K and t is the time in seconds.

For non-magnetic materials, the internal heat generated due to the absorption of microwave power, P, assuming plane wave propagation, is given by:

$$Q = \frac{dP}{dV} = \frac{1}{2}\sigma\left|\overline{E}\right|^2 = \frac{1}{2}\omega\varepsilon''\left|\overline{E}\right|^2 \ (W/m^3), \tag{4.2}$$

where the internal electric field $\overline{E} = \overline{E}(x,y,z,f,\varepsilon)$ is a function of the microwave frequency and the spatial variables, x, y and z; σ is the conductivity of the material at the point (x,y,z); ε'' is the loss factor at that point and $\omega = 2\pi f \ (rad/s)$.

Combining Eq. (4.2) with (4.1), the heating rate is:

$$\frac{dT}{dt} = \frac{\pi f\varepsilon''}{C_p\rho}\left|\overline{E}\right|^2 \ (^\circ K/s) \tag{4.3}$$

Wherever the electric field value $\left|E\right|$ is determined, the heating rate at that point can be calculated by (4.3). However, in the microwave sintering furnace, there are many different materials with different dielectric properties involved so that the electric field value at any point in the furnace is difficult to determine. Also, the heat transfer between materials in the actual heating process is not considered in the above calculation,.

A second, and in our case, preferable approach is to calculate the heating rate of the materials caused by the microwaves, by calculating the power absorbed by the material from the material's attenuation coefficient. Consider a situation of an isotropic solid material with a certain dielectric constant and loss factor which is contained between two infinite plates assumed to be ideal electrical conductors. Uniform plane electromagnetic waves are incident from one side of the material. Then the power ratio at any distance, l, from the front surface of the material is given by:

$$\frac{P_{transmitted}}{P_{incident}} = e^{-2\alpha l} \tag{4.4}$$

where α is the attenuation coefficient. Knowing the incident power in watts and the attenuation coefficient from the transmission loss tests of the material, the power absorbed by the material within a length l can be calculated. Then the energy per unit volume used to heat the material is given by the product of the absorbed power per unit volume and time.

$$Q\Delta t = \frac{dP}{dV}\Delta t \tag{4.5}$$

Consequently, the heating rate can be calculated without knowledge of the electric field strength and dielectric loss factor by using equations (4.4) and (4.5). Interface reflections affecting the power absorption are also accounted for. This is the method to be used in our microwave sintering models.

4.2 Microwave Sintering Furnace

The microwave sintering furnace used at Indexable Cutting Tools. is shown in Fig 4.1. Microwave power at 2.45 GHz is fed into the side of the stainless steel cylindrical cavity through a WR284 waveguide. The cavity load consists of, from the inside out, the samples, an alumina tube, the susceptors and the cerawool insulator. The alumina tube is surrounded by a 25 mm thickness of a susceptor mixture. There are several 8 mm thick graphite plates within the alumina tube forming several layers; each layer holds two or three layers of specimens (the size of the specimen is: 16.5 mm×16.5 mm×11 mm). There is N_2 gas flow inside the alumina tube during the whole process, but air outside the alumina tube. So the oxidizable component in the susceptor mixture can be burned out at high temperature (above 800°C). The entire load is mounted on a rotating plate. The rotation speed is several revolutions per min.

Sketch of Microwave Sintering Applicator

Waveguide

Rotation

Cerawool-775g, 205mm O.D, 155mm I.D, 260mm high

Susceptor Mixture

Graphite-185g/ea, 110mm O.D, 9mm thick

Alumina Tube-660g, 100mm O.D, 6mm thick, 100mm high

Stainless Steel Cavity 300mm O.D, 300mm high
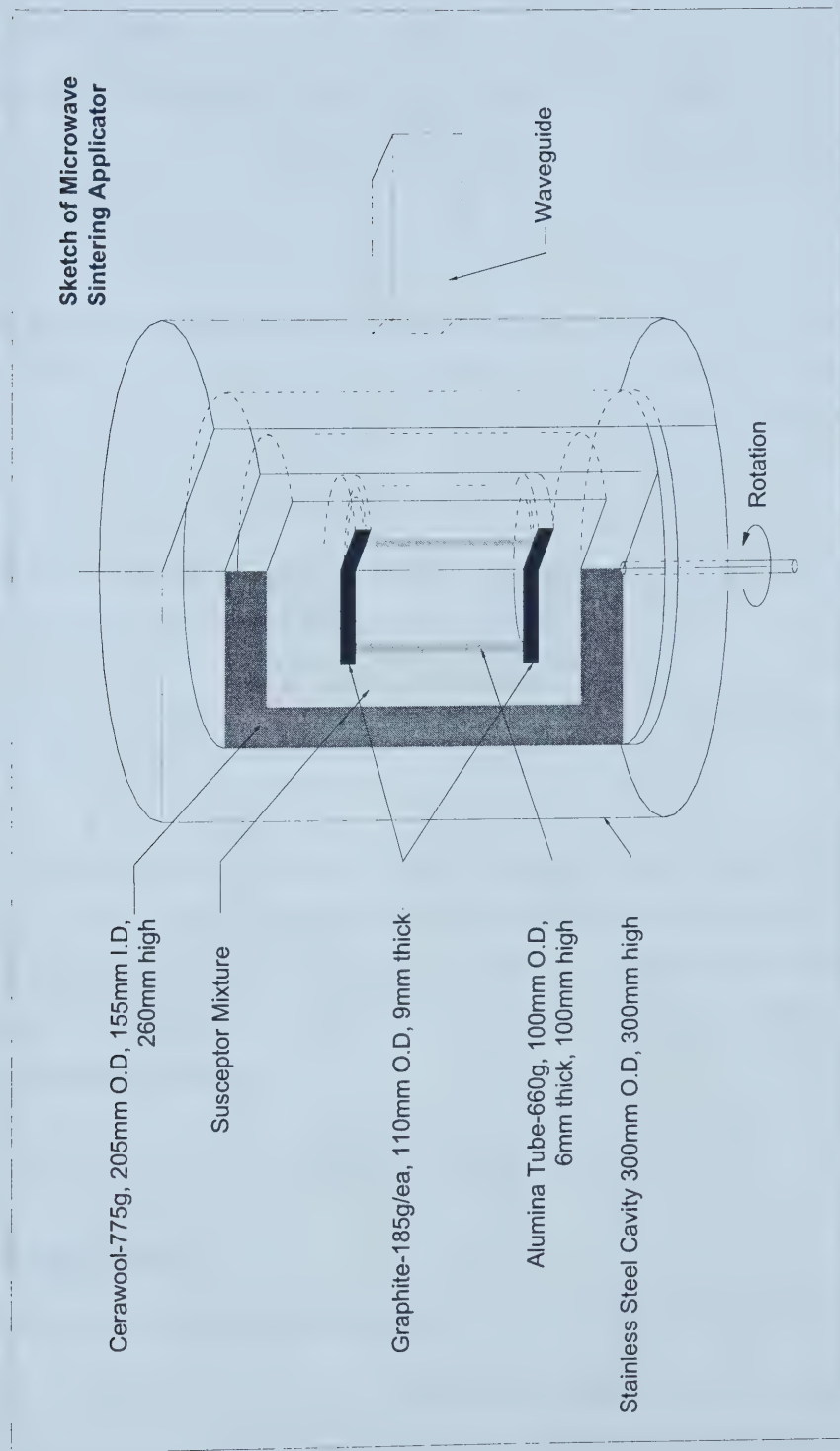
Fig. 4.1 Microwave sintering applicator used by Indexable Cutting Tools.

4.3 Basic Assumptions

Based on this applicator (sintering furnace), we can make the following assumptions:

1. The stainless steel cavity is a good conductor and hence all microwave power will be contained in the applicator.

2. Graphite plates are good conductors, so no microwave power will be propagated through these plates, but heat will be transferred through them. The temperature gradient along the vertical direction in the alumina tube is relatively small and can be ignored.

3. The insulator (cerawool) is a lossless material, for which the microwave attenuation and reflection coefficient are low enough to be ignored.

4. The cavity load is mounted on a rotating platform. It is a cylindrically symmetric system.

As a first approximation, the electric field is uniform in each material across the cross section of the cerawool, susceptors, alumina tube and the samples. Then we can say that the microwave power is uniformly absorbed within each layer of the load across its radial dimension. This approach does not allow one to isolate multiple reflection effects, which may be present in the cavity.

4.4 Microwave Sintering Process Model of Tungsten Carbide

4.4.1 Physical Models

4.4.1.1 Microwave Power Attenuation and Reflection Model for Tungsten Carbide

Consider one layer of the samples separated by two graphite plates in a half cross-section of the sintering furnace model as shown in Figure 4.2. All power values,

designated in the model by P and R, are normalized to percentages of the total input power which itself is given the value of 100%. Power absorption by the cera-wool, the alumina tube and the graphite plates are all relatively small and these can be treated as a small percentage error in the calculation. Thus, most of the power absorption will occur in the susceptor layer and in the tungsten carbide samples. As a result of the low dielectric constant of the susceptor layer, its reflection coefficient is nearly zero.
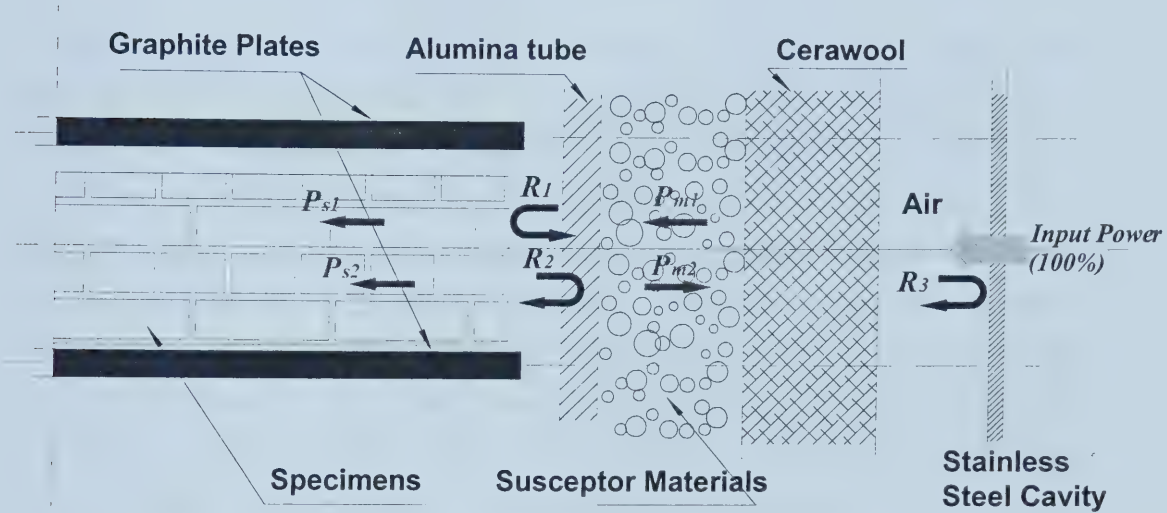
Fig. 4.2 Microwave power attenuation and transmission inside the applicator.

Consider now the microwave power flow through the model's cross-section as shown in Fig. 4.2. Starting at the input with 100% power, a percentage of power, P_{m1}, is absorbed on the first pass through the susceptor layer. The rest of the power is transmitted through the susceptor layer most of which will reach the front face of the sample load. Since the microwave attenuation in the WC/Co samples is very high, all the power entering the samples, say P_{s1}, will be absorbed. Another part of the total power incident on the front face of the sample load is reflected back toward the susceptor layer. This power is designated by R_1. The alumina tube interface causes a re-reflection, say R_2. This causes

further power deposition of P_{s2} in the sample load. Similarly, some of the reflected power, R_1, is also absorbed by the susceptor layer and is designated by P_{m2}. Finally, part of the power reaches the stainless steel cavity wall and is totally reflected (see assumption 1) back toward the susceptor and sample layers. This power reflection, transmission and absorption process continues. In a very short time, a few microseconds, a steady state is reached in which nearly all of the input power is absorbed by the samples and the susceptor layer.

The percentage of power reflected or transmitted at each interface between the materials can be calculated from the reflection and transmission coefficients of each material. These coefficients are themselves determined from the return loss and attenuation data found experimentally as shown in Chapters 2 and 3 in this thesis or from known literature data. For example, R_1 is found from the return loss data shown in Figure 3.3 for the case of WC/Co. P_{m1} and P_{m2} are found from Eq. (4.4) using the attenuation coefficient data for the susceptor material. After about five iterations of these calculations of absorbed power, over 95% input power is absorbed by those materials and the percentage of power deposited in each layer can be estimated. From these values, the total power dissipated per unit volume can be calculated and substituted in Eq. (4.5) to estimate the total internal heat, Q, generated within each material. These data can then be used in the heat generation and heat transfer model described next.

4.4.1.2   Heat Generation and Heat Transfer Model
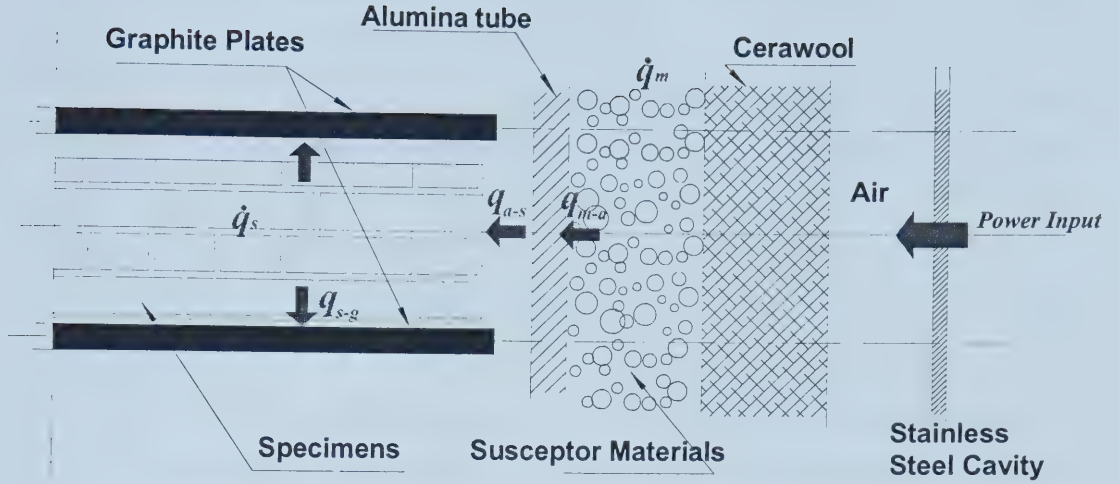
Fig. 4.3 Physical model of heat generation and heat transfer.

A sketch of the heat generation and heat transfer model is shown in Fig.4.3. In a small time interval, Δt, say of 1 second, $\dot{q}_m$ is the microwave power absorbed by the susceptors and $\dot{q}_s$ is the microwave power absorbed by the samples. Since the temperature variation between the samples is relatively small, we can treat it as a bulk material. Also, the temperature gradient in the susceptors and in the alumina tube can be ignored. The heating rate of these parts can be calculated from the absorbed power, the density and the heat capacities given in equation (4.1). There is heat transfer, mainly by conduction, between the susceptors and alumina tube, and radiation heat transfer between the alumina tube and samples. The heat flux from the alumina tube to the alumina tube, q_{m-a}, is

$$q_{m-a} = K_a A_a \frac{T_m - T_a}{l} \qquad (4.6)$$

where T_m and T_a are the absolute temperature of susceptors and alumina, respectively, in K, K_a is the thermal conductivity of alumina in $W/m.K$, l is the thickness of the alumina tube and A_a is the cross-sectional area of the alumina tube. Part of the heat transferred to the alumina is used to heat the alumina tube, and the rest is transferred to the specimens by radiation. The heat transferred from the alumina tube to the specimens, q_{a-s}, is given by:

$$q_{a-s} = \varepsilon \sigma A_s (T_a^4 - T_s^4) \tag{4.7}$$

where T_a and T_s are the absolute temperatures of the alumina tube and the samples in K, ε is the emissivity of alumina, σ is the Stefan-Boltzmann constant ($\sigma = 5.67 \times 10^{-8} \ W/m^2 K^4$) and A_s is the surface area of the samples.

From assumption 2, the graphite plates are perfect conductors and the microwave power absorbed by the graphite plates can be ignored. But there is heat transfer between the samples and graphite plates, which is used to heat the graphite plates. The heat transferred from the samples to the graphite plates, q_{s-g}, is:

$$q_{s-g} = K_g A_g \frac{T_s - T_g}{d} \tag{4.8}$$

where T_s and T_g are the absolute temperature of the samples and the graphite plates in K, A_g is the cross-sectional area of the graphite plates in m^2, K_g is the thermal conductivity of the graphite plates in $W/m.K$ and d is the thickness of the graphite plates.

Neglecting the convective heat transfer and heat loss, the true value of the heat generated, which is used to heat the graphite plates in a small time interval Δt, is:

$$Q_g = q_{s-g} \Delta t \tag{4.9}$$

The energy per unit volume, which is used to heat the samples is

$$Q_s = (\dot{q}_s + q_{a-s} - q_{s-g})\Delta t \tag{4.10}$$

the energy per unit volume used to heat the alumina tube is

$$Q_a = (q_{m-a} - q_{a-s})\Delta t \tag{4.11}$$

and the energy per unit volume used to heat the susceptors is

$$Q_m = (\dot{q}_m - q_{m-a})\Delta t \tag{4.12}$$

Hence, the heating rate of each material in the furnace can be calculated from Eq. (4.1) and (4.9)-(4.12).

4.4.2   Calculation Procedure

The calculation procedure flow diagram is shown in Fig.4.4. The calculations are carried out step by step. Each step has a small time interval (one second). Assume the total power dispersed in the furnace is 85% of the input power during the process. About 15% of the generator's output power is reflected back to the generator because of the overall reflections of the loaded applicator. The output data are used to plot the time-temperature curves.
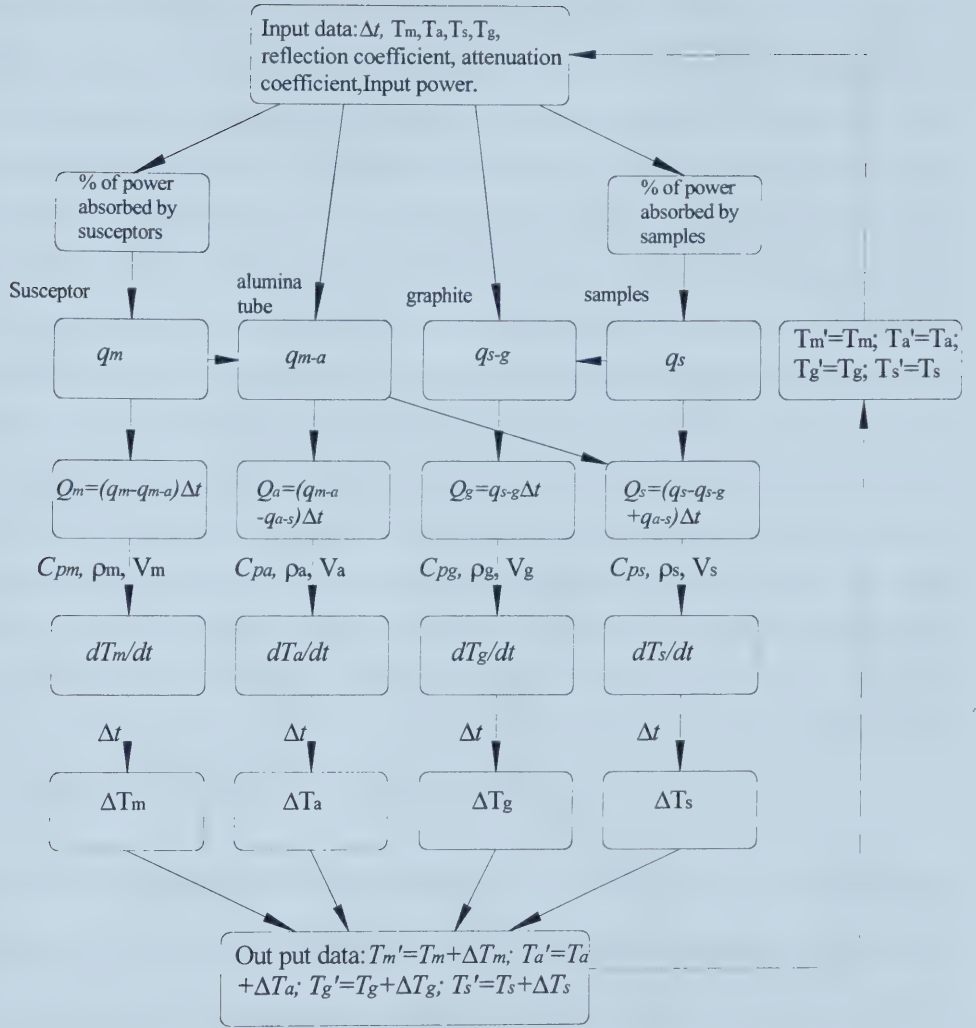
Fig. 4.4 Flow diagram of the calculation procedure.

Since the susceptors start to oxidize above 800°C, their microwave attenuation starts to decrease significantly. Almost all the oxidizable agent will be oxidized above 1000°C and the susceptors become almost pure alumina above 1000°C. Hence, the microwave attenuation properties of the susceptors above 800°C can be estimated from the loss factor and dielectric constant of alumina measured at high temperatures [43] (Appendix VI). Assuming that the oxidization of the oxidizable agent in the susceptors is gradual from 800°C to 1000°C, then the percent of microwave power being absorbed by the 25 mm thick susceptors can be estimated and is shown in Fig.4.5. In the calculations, it is assumed that the susceptor absorption factor decreases linearly from 800°C to 1000°C. Obviously, above 800°C, the amount of power absorbed by the susceptors decreases and more power will be absorbed by the samples. The heating rate of the samples will be higher than that of the susceptors. Once the temperature of the samples is higher than that of the alumina tube inner face, the radiation heat transfer process will be reversed. Heat is transferred from the samples to the alumina tubes and susceptors. However, at high temperature, alumina becomes a good microwave absorber. A significant amount of microwave power will be absorbed by the alumina tube and will heat it directly. Therefore, the heat generation and transfer model has to be corrected for the direct heating of the alumina tube and the reverse heat transfer.

For the WC/Co samples, the heat capacity $C_{ps} = 250 \, J/kg \cdot K$; [44] the density $\rho_s = 3950 \, kg/m^3$. The heat capacity of the susceptor materials is approximately the heat capacity of alumina listed in Appendix I; the density of the susceptors $\rho_m = 560 \, kg/m^3$; the total volume of the susceptors $V_m = 0.001618 \, m^3$; the thickness of the susceptor layer $l = 0.0025 \, m$. The mass of the alumina tube is 660 g, the cross-sectional area $= 0.01 \, m^2$; the emissivity $\varepsilon = 0.5$; the thermal conductivity of alumina K_a is listed in Appendix III. The thermal conductivity of the graphite plates K_g is shown in Appendix IV; the heat capacity of graphite is shown in Appendix II; The thickness of the graphite plates $d = 6 \, mm$, and their cross-section area $= 0.016 \, m^2$. The microwave reflection

coefficients of alumina at different temperatures are calculated from the dielectric data measured by J. Batt et al., [43] shown in Appendix VI.
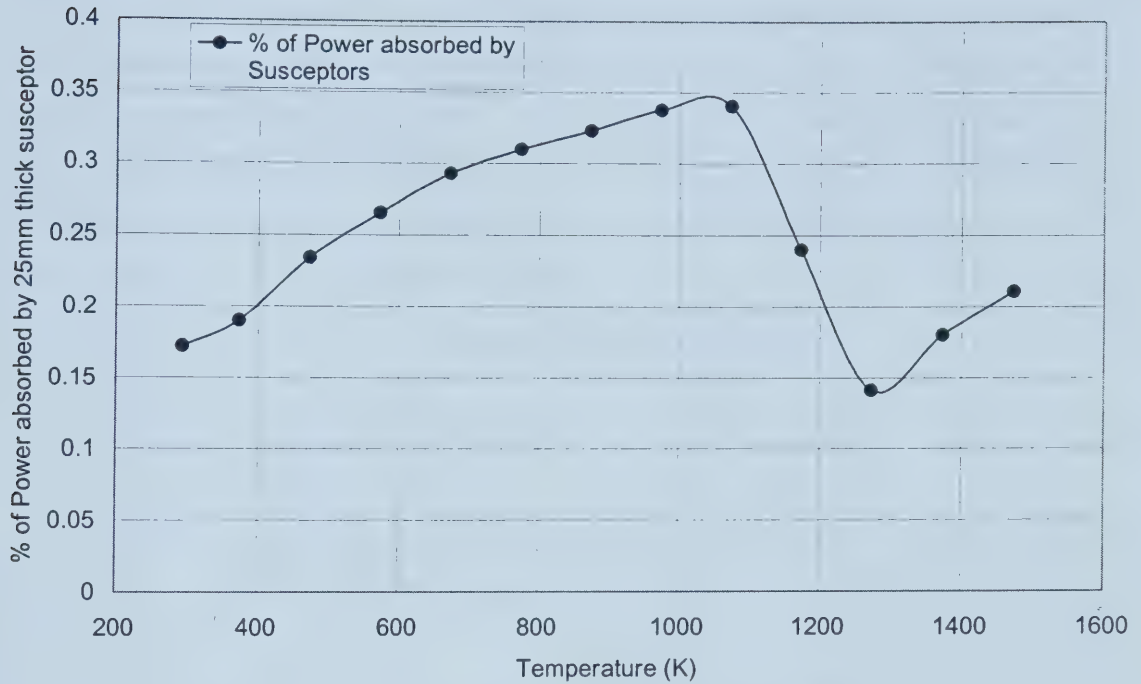
Fig. 4.5 Percentage of power absorbed by a 25 mm thick susceptor layer over the temperature domain.

4.4.3   Time-Temperature Calculation Results and Discussion

The calculation results from the model and the recorded experimental data [45] are plotted in Fig. 4.6. The calculated susceptor temperatures are lower than those from the experiment and the disparity increases with increasing temperature. This disparity is believed to be the effect of not rotating the sample load. In the experimental process, the load in the furnace did not rotate; and the temperature of the susceptors was recorded from the thermocouple which was at the front face of the susceptors facing the microwave

power input waveguide. In this situation, the susceptor are not heated uniformly and the front face susceptor will absorb much more power than the back face susceptors. The high reflection at the front face of the tungsten carbide samples also increases the nonuniformity of the electric field. Hence, significantly higher temperatures are produced at the front face as compared to the back face. From the experimental data, it is observed that when the temperature of the front face susceptors reached 1000°C, the back face susceptor reached a temperature of 500°C. On the other hand, the calculated temperatures of the samples are somewhat higher than that from the experimental data. This discrepancy might come from neglecting the nitrogen gas flow inside the alumina tube and the heat loss from the evaporation of lubricant.

Fig. 4.6 The temperature of WC/Co samples and susceptors over time as calculated from the model and compared with experimental values.

4.5 Microwave Sintering Process Model of Silicon Nitride

Most of the modeling process for the microwave sintering of silicon nitride is similar to that of the tungsten carbide microwave sintering model. However, since the attenuation of silicon nitride is much lower than that of the tungs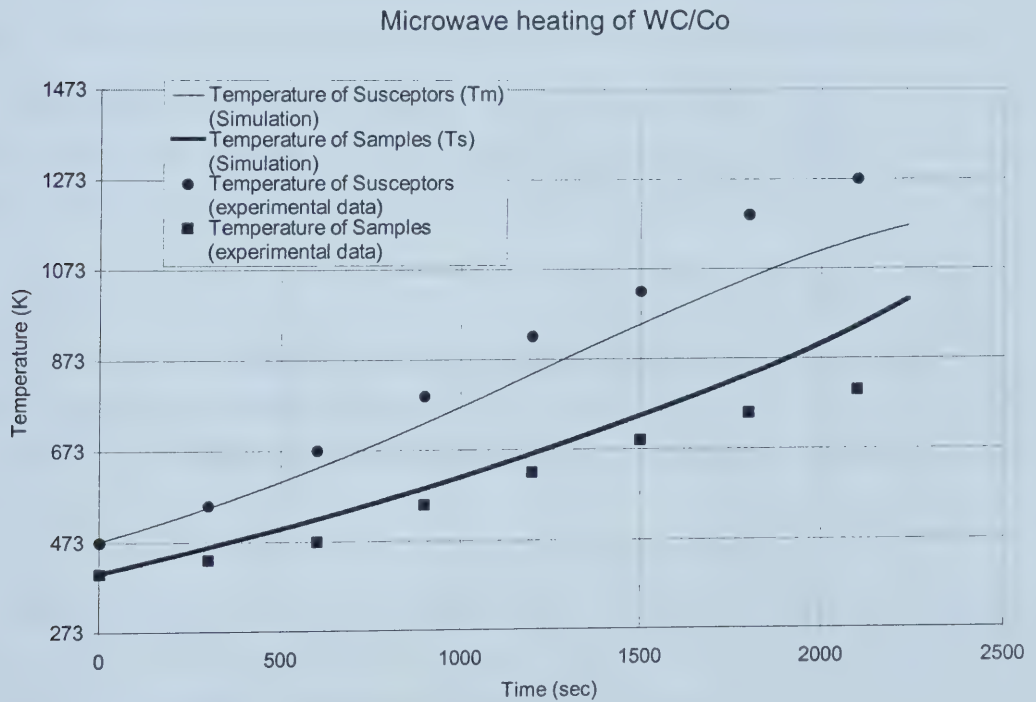ten carbide, most of the power entering the samples will not be absorbed in one pass of the wave front. And, the front face reflection coefficient of silicon nitride samples is much lower than that of the tungsten carbide samples. Hence, more interface reflection and transmission effect have to be considered.

4.5.1   Physical Models

4.5.1.1   Microwave Power Attenuation and Reflection Model for Silicon Nitride

Considering the low attenuation and reflection coefficients of the silicon nitride samples, the whole cross-section of the furnace load (compared to the half cross-section used for the WC/Co case) was analyzed in this physical model as shown in Fig. 4.7.

Power absorption by the cera-wool, the alumina tube and the graphite plates is relatively small and these can be treated as a percentage error in the calculation. Thus, most of the power absorption will occur in the susceptor layer and in the silicon nitride samples. The reflection at the susceptor layer is also neglected because of its low dielectric constant.

Similar to the microwave power attenuation and reflection model of the WC/Co microwave sintering process, all the absorbed power, P, and reflected power, R, are normalized in percentage values relative to the total input power.

Consider now the microwave power flowing through the model's cross-section as shown in Fig. 4.7. Starting at the input with 100% power, a percentage of power, P_{m1}, is absorbed on the first pass through the susceptor layer. The rest of the power is transmitted

through the susceptor layer most of which will reach the front face of the sample load. Since the microwave attenuation in the Si_3N_4 samples is quite low, only part of the power entering the samples, say P_{s1}, will be absorbed. Part of the total power incident on the front face of the sample load is reflected back toward the susceptor layer. This power is designated by R_1. The alumina tube interface causes a re-reflection, say R_2. This causes further power deposition of P_{s2} in the sample load. Similarly, some of the reflected power, R_1, is also absorbed by the susceptor layer and is designated by P_{m2}. The remaining part of the power entering the sample will be transmitted through the sample load and reach the alumina tube and the susceptor layer on the opposite side. Similarly, multiple reflections and absorptions occur and cause the third and fourth part of the power absorbed in the samples, say P_{s3} and P_{s4}. and in the susceptor layer, say P_{m3} and P_{m2}. Part of the power reaches the stainless steel cavity wall and is totally reflected (see assumption 1) back toward the susceptor and sample layers. This power reflection, transmission and absorption process continues. Finally after sufficient passes, all of the input power has been absorbed by the silicon nitride samples or the susceptor layer.

The percentage of power reflected or transmitted at each interface between the materials can be calculated from the reflection and transmission coefficients of each material. These coefficients are themselves determined from the return loss and attenuation data found experimentally as shown in Chapters 2 and 3 in this thesis or from known literature data. After about five iterations of these calculations of absorbed power, the total percentage of power deposited in each layer can be estimated. From these values, the total power dissipated per unit volume can be calculated and substituted in Eq. (4.5) to estimate the total internal heat, Q, generated within each material. These data can then be used in the heat generation and heat transfer model of silicon nitride described next.

4.5.1.2 Heat Generation and Heat Transfer Model for Silicon Nitride

The model for the heat generation and heat transfer during microwave sintering of silicon nitride is similar to that for the microwave sintering of tungsten carbide. At lower

temperatures, the susceptors absorb most of the input power and are heated to higher temperatures than the samples. The alumina tube is heated partly by energy transferred from the susceptors. The temperature of the alumina tube inner face is higher than the temperature of the samples' front face. Hence, heat is transferred from the alumina tube to the samples by radiation. Also, the convective heat transfer inside the alumina tube can be ignored. Assuming that the graphite plates can not absorb any microwave power, the sample temperature should be higher than that of the graphite plates. Heat is transferred from the samples to the graphite plates. The power used to heat the different parts in the furnace are shown in Equations 4.9-4.12. At higher temperatures, because of the oxidation of the susceptors, the microwave absorption properties are changed. The temperature of the samples is significantly higher than that of the inner face of the alumina tube because of the increase of microwave power absorption by the samples. Heat is transferred from the samples to the alumina tube. And, at high temperatures, the alumina tube is no longer a transparent window to the microwaves so part of the microwave power will be absorbed and will heat the alumina tube directly. Similar to the discussion in section 4.4.2, all of these changes have been considered in the microwave sintering Si_3N_4 heat transfer model at high temperatures.

Fig. 4.7 Microwave power attenuation and reflection in the furnace for microwave sintering of silicon nitride

4.5.2   Calculation Procedure

The main procedure for the calculation of microwave sintering of silicon nitride is the same as that for tungsten carbide as shown in Fig. 4.4.

The attenuation properties of silicon nitride come from the measurement results show in section 3.2.2 and its reflection coefficient is calculated from the dielectric constant of silicon nitride using Eq. 3.2. The heat capacity of Si_3N_4 samples is shown in Appendix V; [44] the density of the samples $\rho_s = 1810 \, Kg/m^3$. The heat capacity of the susceptor materials is approximately the heat capacity of alumina listed in Appendix I; the density of susceptors $\rho_m = 560 \, Kg/m^3$; the total volume of the susceptors $V_m = 0.001618 \, m^3$; the susceptor layer thickness $l = 0.0025 \, m$. The mass of the alumina tube is $660 \, g$, the cross-sectional area of the alumina tube = $0.01 \, m^2$; and its emissivity $\varepsilon = 0.5$; the thermal conductivity of alumina K_a is listed in Appendix III. The thermal conductivity of the graphite plates K_g is given in Appendix IV; the heat capacity of graphite is given in Appendix II; the thickness of the graphite plates $d = 6 \, mm$, and their cross-sectional area = $0.016 \, m^2$. The reflection coefficients of alumina at different temperatures are calculated from the dielectric data measured by Batt et al. [43] and shown in Appendix VI.

4.5.3   Calculation Results and Discussion

The calculated results for the model of microwave sintering of silicon nitride and the experimental data for comparison are shown in Fig. 4.8. The input power changed form 500W to 1000W at 4200s. Quite a good match is evident between the calculated temperatures of the samples at the front face and the experimental values up to $1273°K$. At lower temperatures, the simulated values of the susceptors are very close to those of the experimental data, while as the temperature increases to $973°K$, a significant divergence develops. This discrepancy is believed to be the effect of the non-rotation of the load (the experimental data was taken with the load stationary). Non-uniform heating of the susceptors for a stationary load becomes evident at higher temperatures. As stated

before, when the temperature of the susceptors increases to $1073°K$, their heating rate starts to decrease significantly, which is caused by oxidation of the susceptors. As the temperature approaches $1273°K$, the differential between the samples and susceptors tends to zero. The temperature of the samples then begins to exceed that of the susceptors.

Microwave heating of Si_3N_4
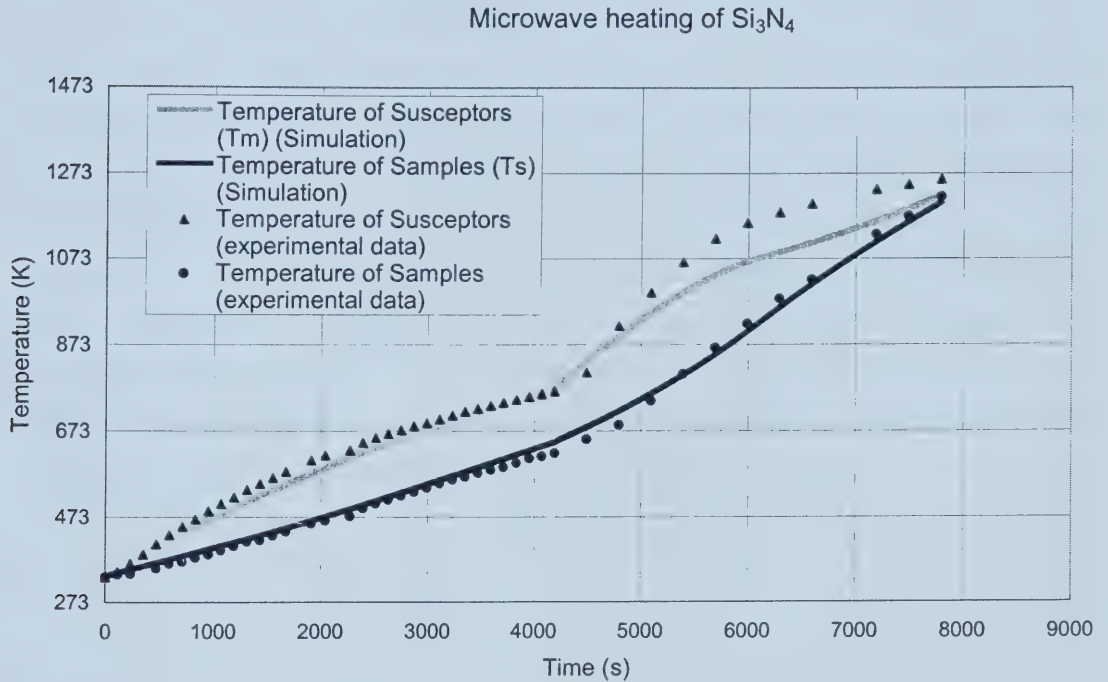
Fig. 4.8 The temperature of Si_3N_4 samples and susceptors over time as calculated from the model and compared with experimental values.

4.6 Process Parameter Influence Determination from the Models

The models are helpful to understand the microwave absorption and heat transfer mechanisms during the sintering process. By changing the values of the design parameters of the load materials, the effect of those parameters can be clearly shown.

4.6.1 Effect of the Thickness of the Alumina Tube Wall

At low temperatures, the alumina tube is a barrier between the "hot" susceptor and the

samples. A large part of the power absorbed by the susceptors is transferred to the alumina tube. As Fig. 4.9 shows, doubling the thickness of the alumina tube for WC/Co microwave sintering will significantly reduce the temperature of the susceptors and the samples. At 2000 seconds, the temperature of the susceptors with a 12 mm thick alumina tube is about $130°K$ lower than that of the susceptors with a 6 mm thick alumina tube. And the temperature of the samples is $100°K$ lower. This is because more power has to be used to heat the alumina tube itself. Hence, more power has been transferred to the alumina tube, but less heat can be transferred from the alumina tube inner face to the samples. If the temperatures at the susceptor-alumina interface in these two situation (6 mm thick alumina tube wall and 12 mm thick alumina tube wall) are the same, the temperature of the inner face of the 12 mm thick alumina tube is much lower than that of 6 mm thick alumina tube. Therefore, the radiation heat transfer from the alumina tube inner face to the front face of the samples will be reduced if the thickness of the alumina tube is doubled. At higher temperatures, this deviation becomes more significant because the radiation heat transfer is the major heating source of the samples.

Fig. 4.9 Effect of the thickness of the alumina tube in the microwave sintering of WC/Co. T_m and T_s are the temperatures of the susceptors and samples with a 6 mm thick alumina tube wall; T_{m2} and T_{s2} are the temperature of the susceptors and samples with a 12 mm thick alumina tube wall.

A similar tube wall thickness effect is found for the sintering of Si_3N_4 as shown in Fig. 4.10. The heating rate of the samples in the 12 mm thick alumina tube is significantly lower than that of the samples in the 6 mm thick alumina tube.
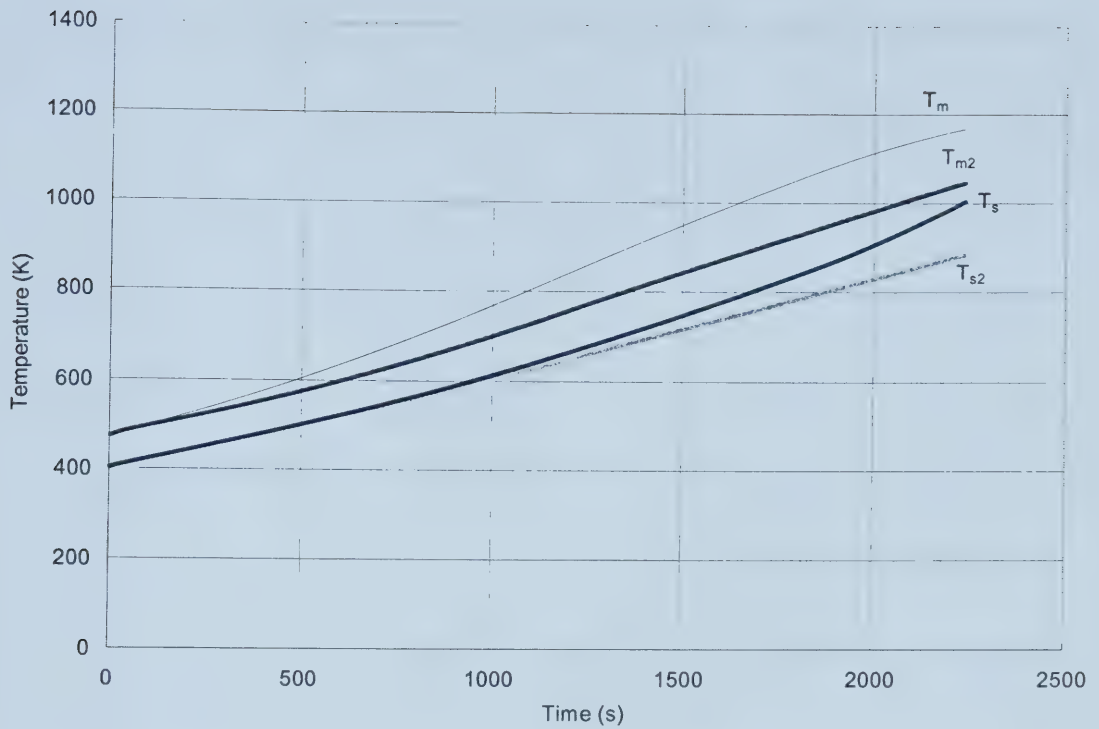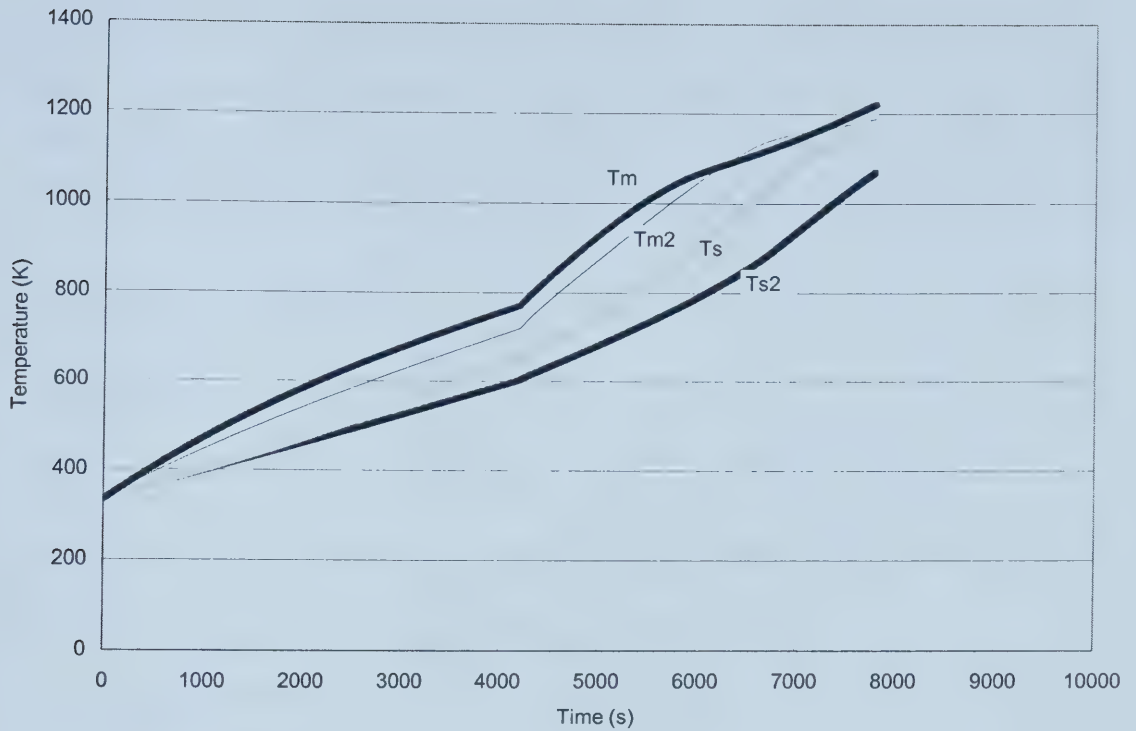
Fig. 4.10   Effect of the thickness of the alumina tube wall in the microwave sintering of Si_3N_4. T_m and T_s are the temperature of the susceptors and samples with a 6 mm thick alumina tube wall; T_{m2} and T_{s2} are the temperature of the susceptors and samples with a 12 mm thick alumina tube wall.

4.6.2   Effect of the Thickness of the Susceptor Layer

Varying the thickness of the susceptors will definitely increase the attenuation of the microwave power through the susceptor layer. More power will be absorbed by the susceptor layer. On the other hand, less power is transferred through the susceptors so that less power is available for absorption by the samples. For the case of double the thickness of the susceptor layer, the temperature versus time curves of the susceptor and the WC/Co samples are shown in Fig. 4.11. The temperature of the samples in a loaded furnace with a 50 mm thick susceptor layer is much lower than that for the case where the samples are

surrounded by a 25 mm thick susceptor layer. However, when the thickness of the susceptor layer increases from 25 mm to 50 mm, the temperature of the susceptor layer itself will decrease. This is because more heat is transferred from the susceptor to the alumina tube and more radiation heat is transferred from the alumina tube to the samples due to the larger temperature gradient between the susceptor layer and the samples .
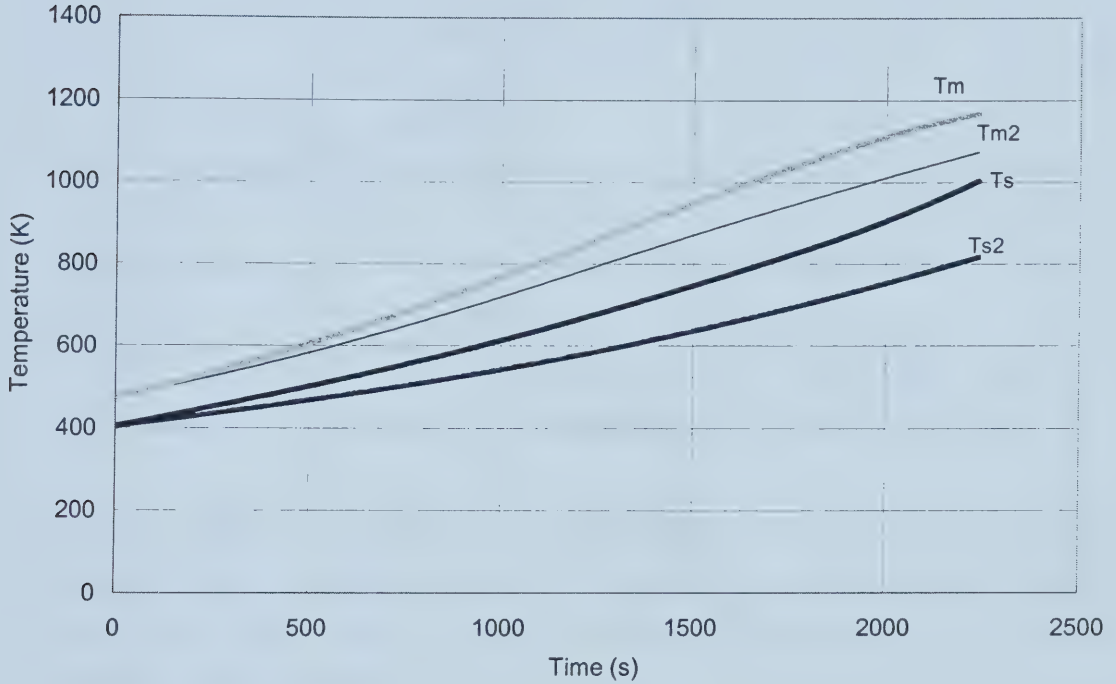
Fig. 4.11   Effect of the thickness of the susceptor layer on WC/Co samples. T_m and T_s are the temperatures of the susceptors and WC/Co samples with a 25 mm thick susceptor layer; T_{m2} and T_{s2} are the temperatures of the susceptors and samples with a 50 mm thick susceptor layer.

A similar susceptor layer thickness effect is found for the microwave sintering Si_3N_4 process as shown in Fig. 4.12. Both the temperatures of susceptors and samples with the 50 mm thick susceptor layer are lower than those with a 25 mm thick susceptor layer.
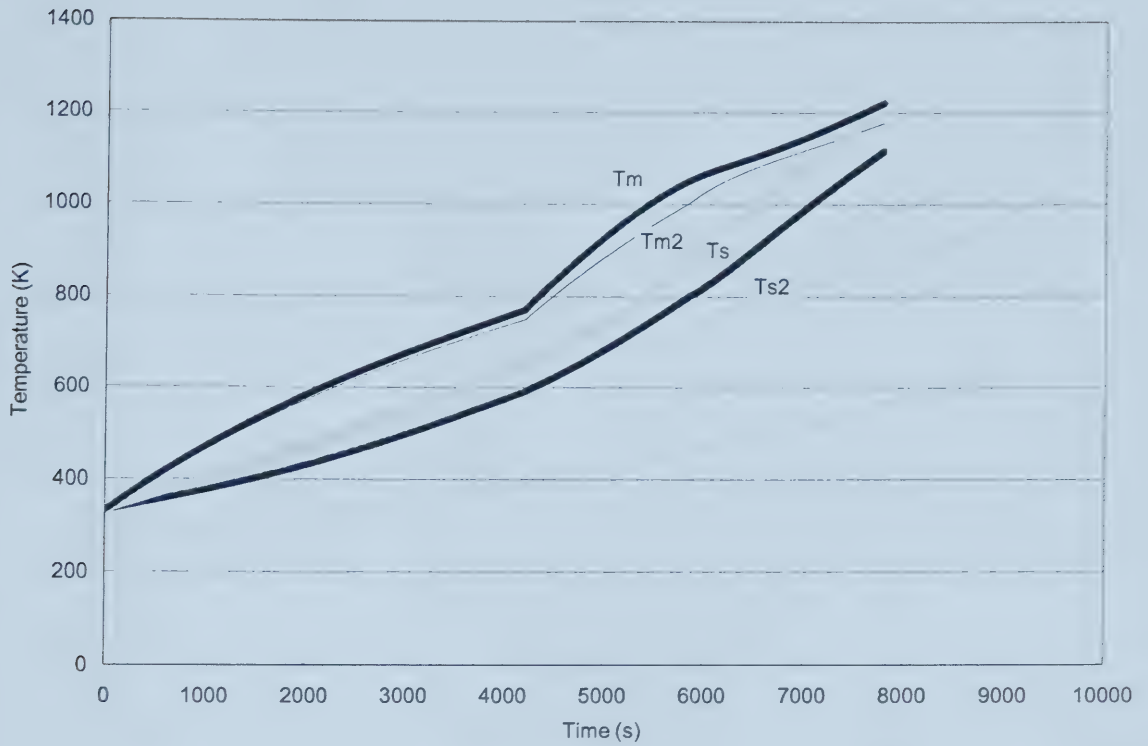
Fig. 4.12   Effect of the thickness of the susceptors in microwave sintering of Si_3N_4 samples. T_m and T_s are the temperatures of the susceptor layer and samples with a 25 mm thick susceptor layer; T_{m2} and T_{s2} are the temperatures of the susceptor layer and samples with a 50 mm thick susceptor layer.

4.6.3   Effect of the Sample Load

Increasing the sample load changes the total surface receiving radiant heat, but it has no influence on the microwave reflection and attenuation model. However, at the same input power level, the heating rate of the samples is lower if the sample load is increased because the same amount of power has to be used to heat more material. Fig 4.13 shows the calculation results for the comparison of 0.8 kg of a WC/Co sample load and a 1.6 kg WC/Co sample load. The temperatures of both the susceptors and the samples with 1.6 kg sample load are lower than those of the susceptors and the samples with a 0.8 kg sample

load.
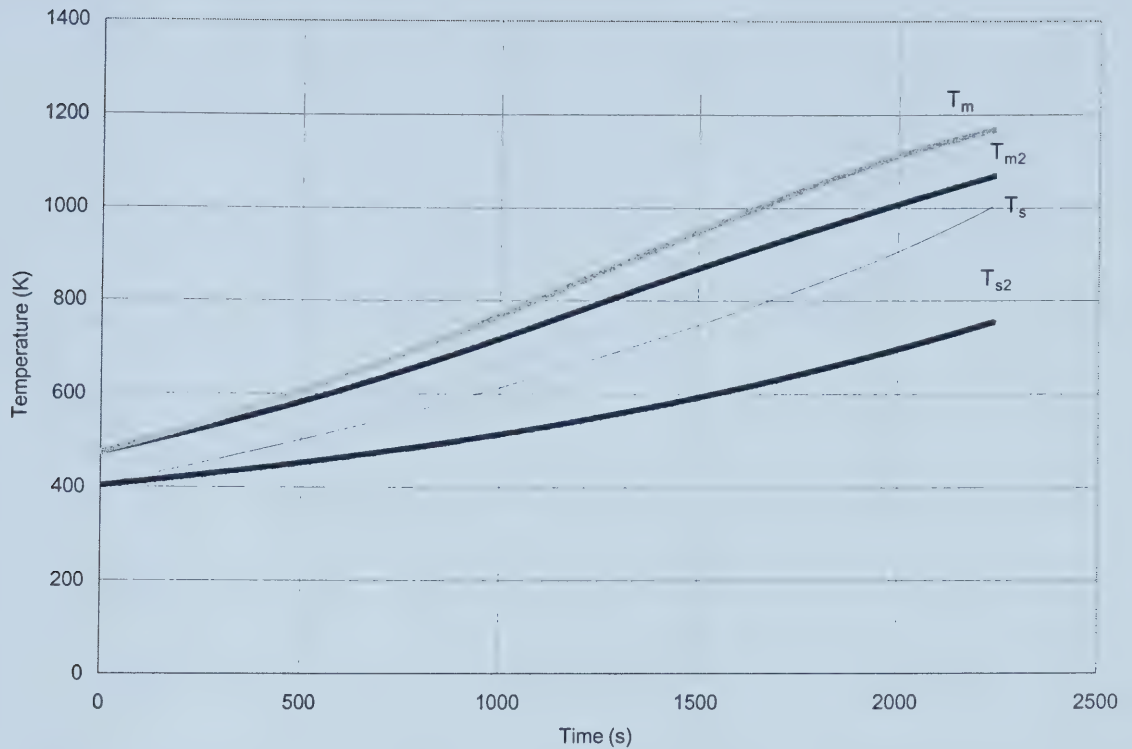
Fig. 4.13   Effect of the sample load. T_m and T_s are the temperatures of the susceptors and samples with a 0.8 kg WC/Co sample load; T_{m2} and T_{s2} are the temperatures of the susceptors and samples with a 1.6 kg WC/Co sample load.

4.6.4   Effect of the Graphite Plates

From the calculation of the WC/Co microwave sintering model, over 60% of the power absorbed by the samples is transferred to the graphite plates. The load of the graphite plates can significantly influence the heating process of the samples. When we remove half of the graphite plates, both the temperature of the susceptors and the temperature of the samples increase as shown in the time-temperature plot in Fig 4.14. At higher temperature, this change becomes clearer. Since less of the power absorbed by the samples is transferred to the graphite plates, the heating rate of the samples is higher. Hence, the temperature differential between the samples and alumina inner face is smaller; and less heat is transferred from the susceptors to the samples. Consequently, the

heating rate of the susceptors is higher.
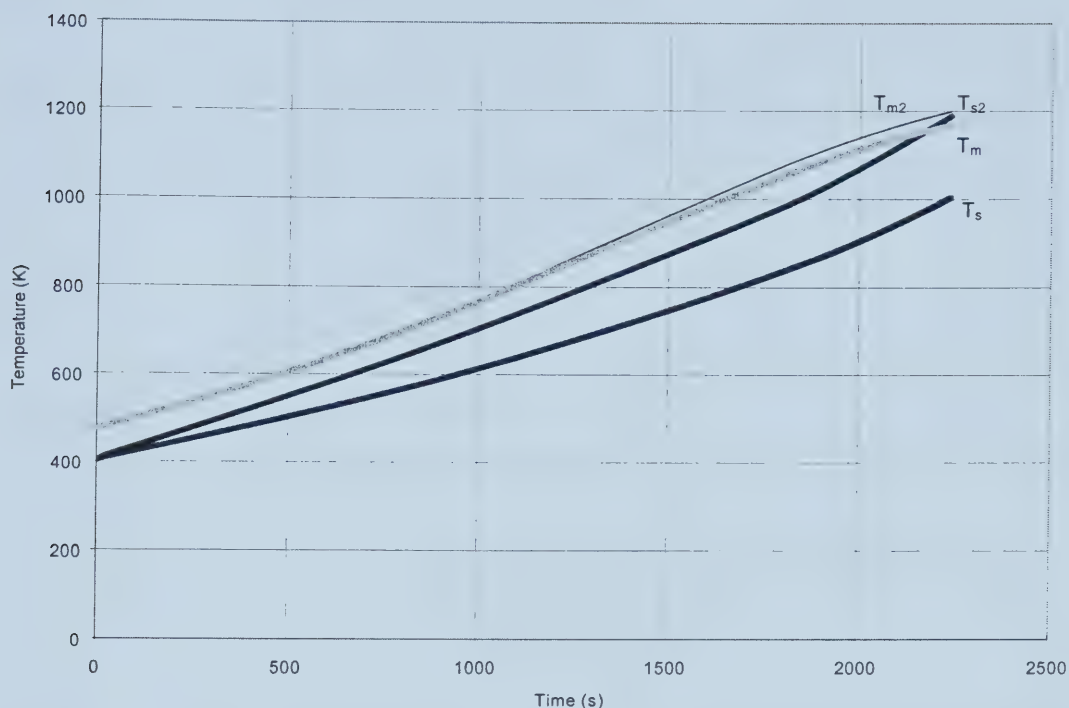
Fig. 4.14   Effect of the graphite load with a WC/Co sample load. T_m and T_s are the temperatures of the susceptors and samples with a 0.42 *kg* graphite load; T_{m2} and T_{s2} are the temperatures of the susceptors and samples with a 0.21 *kg* graphite load.

Modelling results for the microwave sintering of Si_3N_4 also show the same trends as for the WC/Co model as indicated in Fig.4.15. Considering the results shown in Figure 4.14 and 4.15, we can say that the mass ratio of the samples to the graphite is a sensitive parameter for the heating of the samples. The lower the mass ratio, the slower the heating progress of the samples because most heat is transferred to the graphite plates. However, because of the high thermal conductivity of the graphite, the graphite plates are very helpful in minimizing the temperature gradient between the sample loads inside the alumina tube.

Fig. 4.15   Effect of the graphite load on the microwave sintering of Si_3N_4. T_m and T_s are the temperatures of the susceptors and samples with a 0.42 *k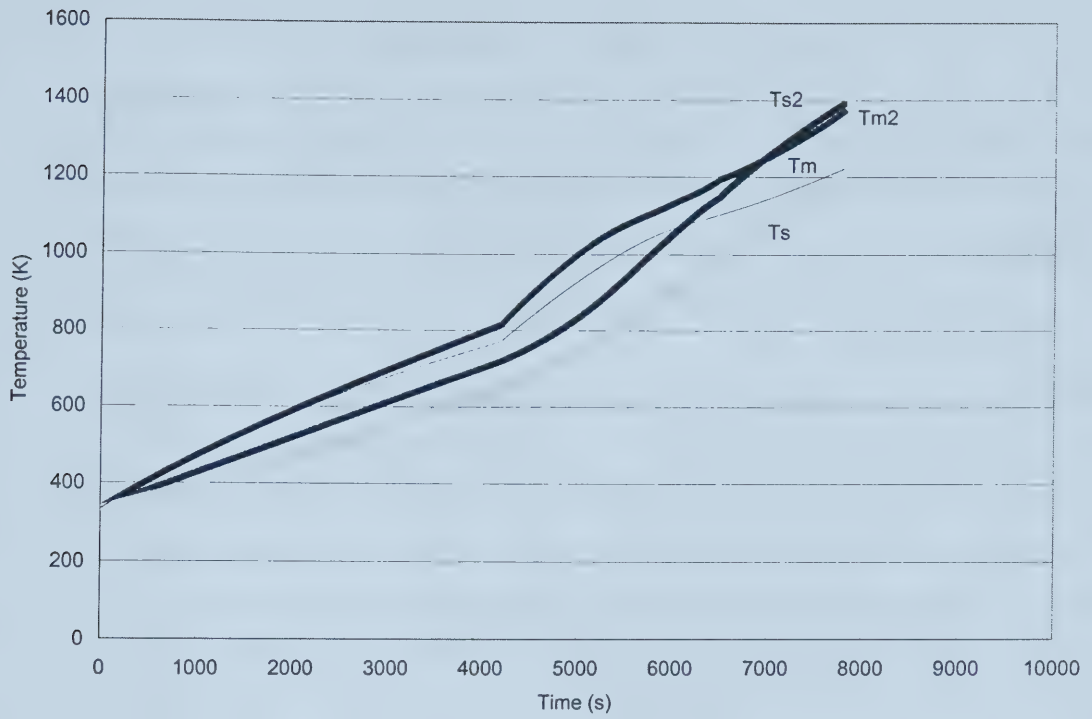g* graphite load; T_{m2} and T_{s2} are the temperatures of the susceptors and samples with a 0.21 *kg* graphite load.

CHAPTER 5   CONCLUSIONS

The attenuation method has been used to measure the attenuation properties of the susceptor materials and the tungsten carbide and silicon nitride green parts of tool bits at different temperatures. From room temperature to 800°C, the microwave attenuation behaviour of these materials can be described as follows:

(1)   Without any gas protection, the attenuation of susceptor mixture materials per unit length increases with an increase in temperature from 0.3 dB/10 mm at room temperature to 0.7 dB/10 mm at 800°C. The increase of attenuation is approximately linear from 20°C to 500°C then levels off. With a nitrogen or argon gas flow around the samples in the waveguide, the attenuation of susceptor mixture materials per unit length kept increasing linearly from room temperature to 800°C.

(2)   A very interesting phenomenon was found in the attenuation test of the susceptor mixture with gas flow. When the mixture cooled down from high temperature to room temperature, its attenuation remained at a very high value (about 5% lower than that at 800°C) which means some permanent change occurred during the process. This change is believed to be the consolidation of the powders at the susceptor surface, and hence an increased electrical conductivity of the susceptors. However, this surmise has not been proven.

(3)   The attenuation tests of tungsten carbide green parts were carried out with nitrogen gas flow around the samples. No significant trend was found during the heating process. The attenuation per unit length of the tungsten carbide green parts was around 10 dB/10 mm which means two or three layers (30~50 mm thick) of this material will absorb almost all the incident microwave power. However, the front face reflection of the tungsten carbide is also very high.

About 80% incident power is reflected back from this interface at all temperatures from room temperature to 800°C.

(4) The attenuation per unit length value of the silicon nitride sample at room temperature is 0.12 dB/10 mm. Because of the evaporation of the lubricant in the green parts, the attenuation decreases to 0.06 dB/10 mm at 500°C. Above 600°C, the attenuation of the material increases very significantly and linearly.

The swept frequency test was employed to measure the dielectric constant of the silicon nitride green samples. The dielectric constant of the material is 3.50±0.02 at room temperature.

Based on the measurement data and general assumptions, models of microwave heating of the materials in the microwave-sintering furnace were developed. The simulated process temperature-time curves are close to the experimentally determined time-temperature curves taking into account that the experiments were done without rotation. The models show that:

(1) At low temperature, most of the microwave power was absorbed by the susceptor mixture and this heats the susceptor layer to higher temperatures than those of the samples. The alumina tube is almost transparent to the microwaves. Part of the heat is transferred from the susceptors to the alumina tube. There is heat transfer mainly by radiation from the alumina tube inner face to the front face of the samples. The graphite plates between the samples are also heated by heat transferred from the samples.

(2) Because of the oxidation of the oxidizable constituent in the susceptor mixtures between 800°C and 1000°C, the microwave attenuation through the susceptor layers decreases significantly over this range. Above 1000°C, most of the power will be absorbed by the samples. Hence, the heating rate of the samples is higher than that of

the susceptors. Eventually, the temperature of the samples exceeds that of the susceptors. Consequently, the heat-transfer process reverses: Heat is transferred from the samples to the alumina tube and the susceptor at high temperature. However, at higher temperature, the alumina tube will also absorb a significant amount of microwave power.

By changing the parameters of the materials involved in the process, we can estimate the effect of these materials on the heating process. The influence of the process parameters is summarized as follows:

(1) The alumina tube is a heat barrier at low temperature. When the thickness of the alumina tube is increased, more power has to be used to heat the alumina tube and a larger temperature difference has to be present across the alumina. The heating rates of the susceptors and samples decrease with an increase of the alumina tube wall thickness.

(2) Increasing the thickness of the susceptor layer will increase the total amount of power being absorbed by the susceptors. The heating rate of the samples will be significantly reduced because of the thickening of the susceptor layer.

(3) Adding more sample load will slow down the heating progress. Even with an increase of the total surface area of the samples, the amount of total power absorbed by the samples remains almost the same because the transferred radiation heat is not a major heating source of the samples at low temperature, especially for the WC/Co samples.

(4) If the mass ratio of the sample load to the graphite plates is not high enough, most of the heat generated in the samples will be transferred to the graphite plates. By decreasing the load of the graphite plates, we can increase the heating rate of the samples very significantly. However, because of the high thermal conductivity of the graphite, the graphite is very helpful in minimizing the temperature gradients within

the sample loads. Minimizing the thickness of the graphite plates and increasing the thermal conductivity in the radial direction would optimize the heating process.

The work reported in this thesis is based on an understanding of the microwave interaction with the materials and a heat transfer model developed therefrom. This work will contribute substantially to the subsequent development of the microwave sintering of both ceramics and hard metals.

BIBLIOGRAPHY

[1] T. Gerdes, M. Willert-Porada, "Microwave sintering of metal-ceramic and ceramic-ceramic composites", Mat. Res. Soc. Symp. Proc, Vol. 347, pp. 531-537, 1994.

[2] M. Willert-Porada, " Microwave sintering of hard metals", Int. J. of Refractory Metals & Hard Metals, 16, pp. 409-416, 1998.

[3] Ruth Wroe, " Microwave sintering coming of age", MPR, pp. 24-28, July/August 1999.

[4] M. Willert-Porada, " Microwave reaction sintering of tungsten carbide cobalt hard metals", Mat. Res. Soc. Symp. Proc. Vol. 430, pp. 175-180, 1996.

[5] Xiaolin Chen, Reginald L. Eadie, " Microstructural development during microwave sintering of cemented tungsten carbide", PMMTEC'99, part 10, pp. 63-72, 1999.

[6] Dinesh Agrawal, "Metal Parts from Microwaves", Materials World, pp. 673-673, Nov, 1999.

[7] Thomas E. Hale "Sintering of cemented carbides", Production Sintering Practices, pp. 385-389, 1988.

[8] R. J. Nelson and D. R. Milner, "Densification processes in the tungsten carbide-cobalt system" Powder Metallurgy, Vol. 15, No. 30, pp. 23-41, 1972.

[9] R. F. Snowball and D. R. Millner, "Densification processes in the tungsten carbide-cobalt system", Powder Metallurgy, Vol. 11, pp. 346-363 No.21, 1968.

[10] Kazuki Okada, "Effect of Cr_3C_2 addition on the sintering of cemented carbide", PM2TEC98, Las Vegas, 1998.

[11] D. F. Carroll and R. T. Fox, " Processing considerations for superfine WC powders with cobalt additions", Metal powder industries federation, advances in powder metallurgy & particulate materials-1998. Volume 1, Parts 1-4 (USA), pp. 1.61-1.74, June 1999.

[12] R. K. Sadangi, "Grain growth inhibition in liquid phase sintered nanophase WC/Co alloys", International Journal of Powder Metallurgy (USA), vol. 35, no. 1, pp. 27-33, Jan.-Feb. 1999.

[13] J. R. Davis editor, "Cemented carbides", Tool Materials, an ASM Specialty Handbook, published by ASM International, materials park, Ohio, USA, pp. 36-57,

1995.

[14] W. D. Schubert, A. Bock & B.Lux, "General Aspects and Limits of Conventional Ultrafine WC Powder Manufacture and Hard Metal Production", Int. J. of Refractory Metals & Hard Materials, 13, pp. 281-296, 1995.

[15] L. Gao and P. Seegopaul, "Developments in nanograin and micrograin WC-Co composite powder technology", Metal Powder Industries Federation, Advances in Powder Metallurgy & Particulate Materials-1998. Volume 1, Parts 1-4 (USA), pp. 1.29-1.37, June 1999.

[16] Kenneth JA Brookes, 'Sintering techniques show promise for ultrafine WC/Co", Metal Powder Report, Vol35, No.4, pp. 10-14, 2000.

[17] Thomas J. Drozda, "Ceramic Tools Find New Applications", Manufacturing Engineering, May, 1985.

[18] O. Yeheskel, Y. Gefen, "The Effect of the α Phase on the Elastic Properties of Si_3N_4", Materials Science and Engineering, 71 pp. 95-99, 1985.

[19] M. Mitomo, "In Situ Microstructure Control in Silicon Nitride Based Ceramics", Advanced CeramicsII, pp.147-161, 1986.

[20] Prasad S. Apte and William D. MacDonald, "Microwave Sintering Kilogram Batches of Silicon Nitride", Microwaves: Theory and Application in Materials Processing III, pp.55-62, 1995.

[21] J. O. Kiggans, "Processing of Complex Sintered Reaction-bonded Silicon Nitride Parts by Microwave Heating", Microwave: Theory and Application in Materials Processing II, pp. 269-276, 1993.

[22] David M. Pozar, "Microwave engineering", Addison-Wesley publishing company, 1990.

[23] W. Stephen Cheung, Frederic H. Levien, "Microwaves made simple, principles and applications", Artech house Inc., 1985.

[24] David E. Clark, Microwave Processing of Materials, Microwave: Theory and Application in Materials Processing IV, pp. 61-96, 2000.

[25] L. A. Dissado and R. M. Hill, " What Form of Motion Gives Rise to Dielectric Response at Microwave Frequencies?", Microwave: Theory and Application in

Materials Processing IV, pp. 99-106, 2000.

[26] Robert F. Schiffmann, "Principles of Industrial Microwave and RF Heating", Ceramic Trans., Vol. 80, Microwave: Theory and Application in Materials Processing IV, pp. 41-60, 2000.

[27] R. Bartnikas, "Engineering dielectrics volume II. An electrical properties of solid insulating materials: molecular structure and electrical behavior", ASTM Special Technical Publication, 1983.

[28] V. Pohl, "Correction procedures for the measurement of permitivities with the cavity perturbation method", Journal of microwave power and electromagnetic energy, Vol. 30 No.1, pp. 10-26, 1995.

[29] Weiguo Xi, R. W. Tinga, "A High Temperature Microwave Dielectrometer", Ceramic Trans., Vol. 21, Microwaves: Theory and Application in Materials Processing, pp. 215-224, 1991.

[30] W. R. Tinga, "Overview of single frequency dielectrometer", High temperature dielectrometer user manual, Microwave Power Lab, University of Alberta, 1999.

[31] Leong, K., J. Mazierska, and J. Krupka, "Measurements of unloaded Q-factor of transmission mode dielectric resonators", MWSYM 97 1639-1642, Vol. 3, 1997.

[32] MicroWear Corporation, Inventor: Apte, Prasad Shrikrishna; Morris, Larry Roy, "Microwave sintering process", US patent, Patent Number US5736092.

[33] W. R. Tinga, " MicroWear Report", Microwave Power Lab., University of Alberta, 1999.

[34] W. R. Tinga and E. M. Edwards, Dielectric Measurements Using Swept Frequency Techniques, Journal of Microwave Power, 3(3), 1968.

[35] David K. Wong, Microwave dielectric constants of metal oxides at high temperatures, Thesis of Master of Science, University of Alberta, 1975.

[36] J. R. Thomas, Jr., "Importance of Dielectric properties in Modelling of Microwave Sintering of Ceramics", Ceramic Trans., Vol. 59, Microwaves: Theory and Application in Materials Processing III, pp. 297~304, 1995.

[37] Y. L. Tian, "Dynamic Model for Electromagnetic Field and Heating Patterns in Loaded Cylindrical Cavities", Microwaves: Theory and Application in Materials

Processing III, pp. 261~268, 1995.

[38] A. Birman, "Modeling of Multi-frequency Microwave Sintering of ZnO Ceramic", Ceramic Trans., Vol. 59, Microwaves: Theory and Application in Materials Processing III, pp. 297~304, pp. 305~310, 1995.

[39] Rajiv K. Singh, "Thermal Analysis of Microwave Processing of Ceramics", Ceramic Trans., Vol 21, Microwaves: Theory and Application in Materials Processing, pp. 247~255, 1993.

[40] R. Borchert, M. Willert-Porada, "Pressureless Microwave Sintering of Metal-Ceramic Functionally Gradient Materials", Ceramic Trans., Vol. 80, Microwaves: Theory and Application in Materials Processing IV, pp. 491~498, 2000.

[41] Lasri J., "Energy Conversion During Microwave Sintering of a Multiphase Ceramic Surrounded by a Susceptor", Am. Ceramic Soc. 83 [6], pp. 1465, 2000.

[42] Wayne R. Tinga, "Microwave Material Interactions and Process Design Modeling", Ceramic Trans., Vol 21, Microwaves: Theory and Application in Materials Processing, pp. 29~41, 1993.

[43] J Batt, J G P Binner, T E Cross, N R Greenacre, M G Hamlyn, R M Hutcheon, W H Sutton and C M Weil, "A Parallel Measurement Programme in High Temperature Dielectric Property Measurements: An Update", Ceramic Trans., Vol. 36, Microwaves: Theory and Application in Materials Processing III, pp. 243-250, 1995.

[44] Kenneth J A Brookes, "World Directory and Handbook of Hard metals and Hard Materials", fifth edition, 1992.

[45] Rob Roy, Dave Allan, MicroWear Experimental Report on Microwave Sintering of WC/Co and Si_3N_4, Edmonton, AB, Canada, 1999.

[46] Frank P. Incropera and David P. De Witt, Fundamentals of Heat Transfer, John Wiley & Sons Inc., 1981, Appendix A.

Appendix I Heat Capacity of Alumina[46]

Temperature T (°K)	Heat Capacity C_p ($J/kg.°K$)
400	940
600	1110
800	1180
1000	1225

Simulation formula:

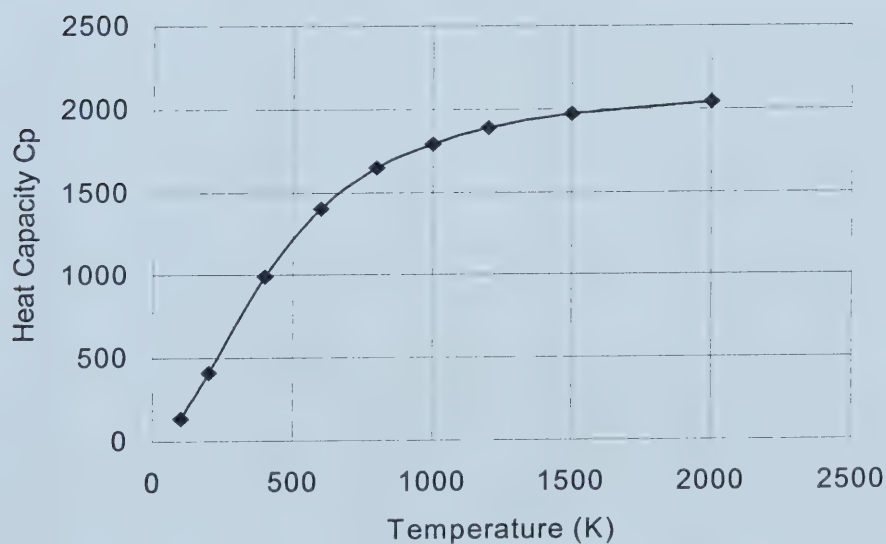$$C_p = -1.8229 \times 10^{-9} T^4 + 6.67 \times 10^{-6} T^3 - 9.2396 \times 10^{-3} T^2 + 5.9708T - 350$$

Heat Capacity of Alumina

Appendix II   Heat Capacity of Graphite [46]
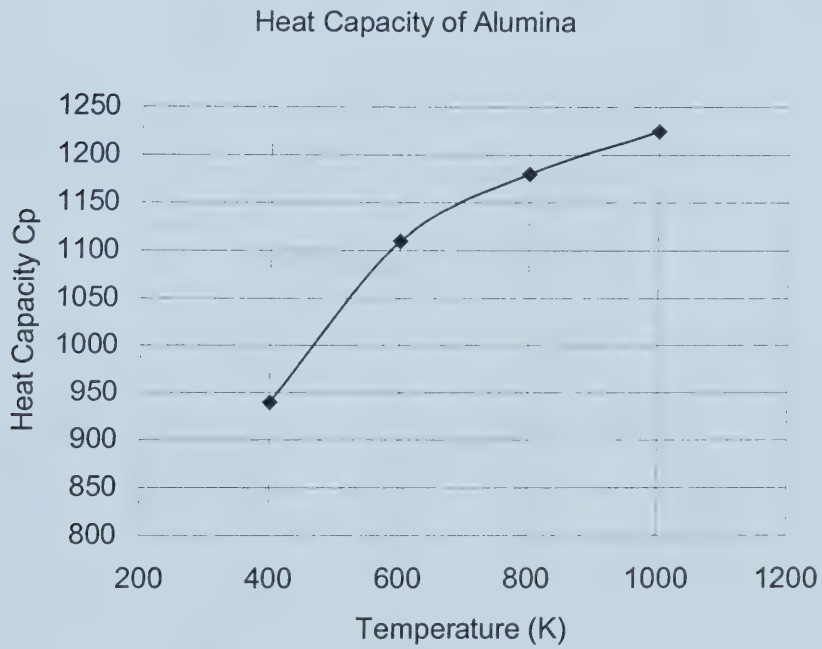
Temperature T (°K)	Heat Capacity C_p (J/kg.°K)
100	136
200	411
400	992
600	1406
800	1650
1000	1793
1200	1890
1500	1974
2000	2043

Simulation formula:

$$C_p = 5.9 \times 10^{-7} T^3 - 2.7273 \times 10^{-3} T^2 + 4.2843T - 331.21$$
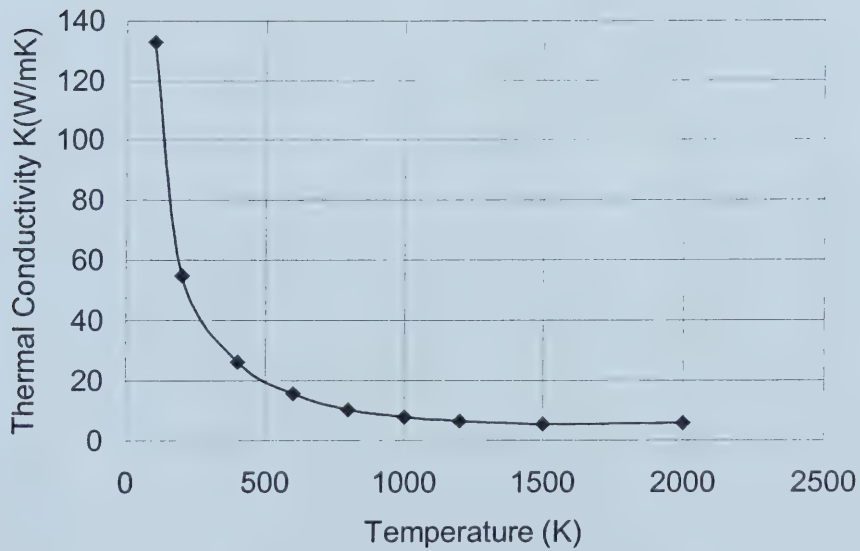
Heat Capacity of Graphite

Appendix III Thermal Conductivity of Alumina [46]

Temperature T (°K)	Thermal Conductivity K($W/m.°K$)
100	133
200	55
400	26.4
600	15.8
800	10.4
1000	7.85
1200	6.55
1500	5.66
2000	6.00

Simulation formula:

$$K = -1.1089 \times 10^{-13} T^5 + 5.3937 \times 10^{-10} T^4 - 1.0358 \times 10^{-6} T^3 + 1.0042 \times 10^{-3} T^2 - 0.51425T +$$
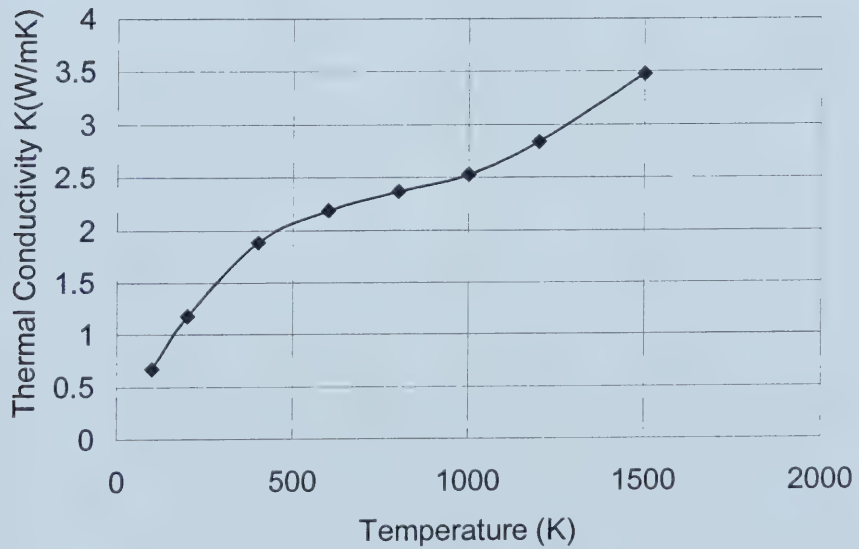

Thermal Conductivity of Alumina

Appendix IV   **Thermal Conductivity of Graphite** [46]

Temperature T (°K)	Thermal Conductivity K($W/m.°K$)
100	0.67
200	1.18
400	1.89
600	2.19
800	2.37
1000	2.53
1200	2.84
1500	3.48

Simulation formula:

$$K = -4.3596 \times 10^{-16} T^5 - 3.1198 \times 10^{-13} T^4 + 6.7181 \times 10^{-9} T^3$$
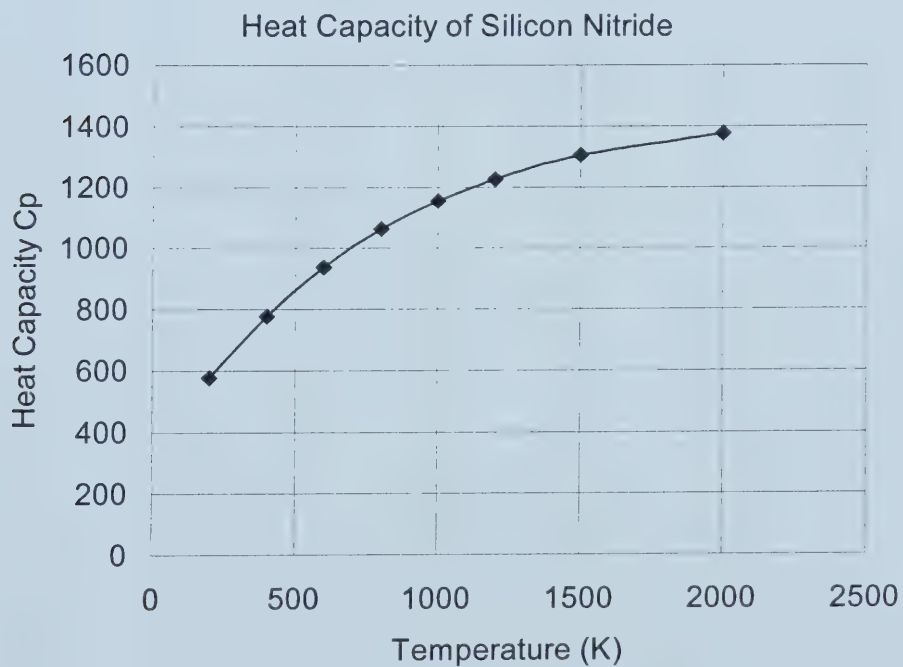$$-1.2342 \times 10^{-5} T^2 + 9.1107 \times 10^{-3} T - 0.20094$$

Thermal Conductivity of Graphite

Appendix V   Heat Capacity of Silicon Nitride [46]

Temperature T ($°K$)	Heat Capacity C_p ($J/kg.°K$)
200	578
400	778
600	937
800	1063
1000	1155
1200	1226
1500	1306
2000	1377

Simulation formula:

$$C_p = -2.6481 \times 10^{-11} T^4 + 2.1908 \times 10^{-7} T^3 - 7.77 \times 10^{-4} T^2 + 1.416T - 323.68$$

Heat Capacity of Silicon Nitride

Appendix VI   Dielectric Constant and Loss Factors of Alumina [43]

Temperature (°C)	Dielectric Constant	Loss factor
20	9.6	0.01
100	9.7	0.02
200	9.8	0.03
300	9.9	0.05
400	10.0	0.1
500	10.1	0.2
600	10.2	0.3
700	10.3	0.7
800	10.5	1.1
900	10.6	2.3
1000	11.0	3.1
1100	11.5	4.1
1200	12.0	5